Characterization of the Anti-Coincidence Shield of the Spectrometer SPI of the INTEGRAL Satellite

Charakterisierung des Antikoinzidenzsystems des Spektrometers SPI des Satelliten INTEGRAL

A thesis submitted for the degree of
Bachelor of Science

Felix Schmuckermaier

03669155

November 14, 2018

Supervisor: Prof. Dr. Roland Diehl

Contents

List of Figures

List of Tables

List of Acronyms

ACS	Anticoincidence Shield
BGO	Bismuth germanate
FoV	Field of view
FEE	Front-end electronic box
GRB	Gamma-ray burst
INTEGRAL	INTErnational Gamma-Ray Astrophysics Laboratory
MLE	Maximum Likelihood Estimation
PMT	Photomultiplier tube
SPI	SPectrometer on Integral

1. Introduction

Gamma-ray astronomy covers all astronomical objects and phenomena that emit gamma rays. Gamma rays are the most energetic type of electromagnetic radiation and in the context of astronomy are defined as having photon energies above around 100 keV. A main field of gamma-ray astronomy is the investigation of gamma-ray bursts (GRBs) (Vedrenne and Atteia, 2009, Chapter 1). GRBs are short and highly energetic flashes of gamma rays. They are the brightest known electromagnetic events in the universe and can last from less than a second to up to a few hours. They were first discovered in 1967 by the VELA military satellites and officially announced in 1973. These satellites were supposed to detect nuclear explosions but discovered the first GRB by accident. Since then, a lot of progress in research has been made, but there are still several unsolved questions regarding the nature of GRBs. Hence the further exploration of GRBs is one of the major scientific tasks within the field of gamma-ray astronomy.

GRBs are transient events and it is impossible to predict their appearance. Most conventional instruments used in gamma-ray astronomy are space telescopes with a limited field of view (FoV) of only a few degrees. This is necessary to achieve a sufficient spatial resolution, but restricts the number of possible GRB detections, because they can only be seen if they appear inside the instruments field of view. In order to increase the rate of GRB detections, omnidirectional detectors are of advantage. These types of detectors have no exceptional field of view and are able to detect GRBs coming in from almost any direction. The most recent and impressive example to demonstrate how relevant these detectors are for astronomy is the gravitational wave event GW170817 and the associated gamma-ray burst GRB170817A (Abbott et al., 2017). On the 17th of August 2017, the Advanced LIGO and Virgo detectors registered a gravitational wave signal originating from a binary neutron star merger. The Gamma-ray Burst Monitor on the NASA satellite Fermi and the Anti-Coincidence Shield (ACS) of the Spectrometer for INTEGRAL (SPI) mounted on the International Gamma-Ray Astrophysics Laboratory (INTEGRAL) of ESA were both able to independently detect a short GRB 1.7 seconds after GW170817. This gives the first direct evidence for an origin model of short GRBs. It confirms that binary neutron star mergers and their associated kilonovae are progenitors of short GRBs, which marks a breakthrough in multimessenger astronomy.

The ACS, initially devoted for reducing the cosmic-ray background of SPI, turned out to be an excellent tool to study GRBs and other high-energy phenomena. Spectral information is solely given by an energy threshold of the detectors. This way, the ACS detects particles coming in from outside of SPI's FoV with energies higher than the set threshold. The threshold value was determined by a ground calibration. With INTEGRAL, the ACS is in space for more than 16 years and since the Earth calibration, the detectors were exposed continuously to radiation, which may had a large impact on the performance of the ACS as a GRB detector. In this thesis, the calibration of the 91 individual scintillation detectors is investigated, and analyzed for possible changes in the instruments response. The thesis is structured in the following way: The INTEGRAL space observatory as a whole and in particular the ACS is pictured in chapter 2. It starts with a short overview of the INTEGRAL mission, and covers a brief history, the scientific goals and the instruments on board. Next, the structure and function of SPI and the ACS are described in detail. An explanation of the function principle of scintillation detectors, the material used for it and their calibration on Earth is given. Chapter 3 provides a depiction of the ACS data. This includes an overview of the main background and sky sources, examples of the data used in this thesis, and a thorough description of the data emergence process. This results in a model used for the later analysis. The chapter ends with a comparison of different fitting methods. In chapter 4 the analysis is presented. Different models for the cosmic-ray spectrum are tested and approaches for improvement are discussed. The analysis then focuses on the examination of a potential change over time of the detectors properties. Finally chapter 5 provides a summary and draws a conclusion.

2. The Space Observatory INTEGRAL

2.1 Mission Overview

INTEGRAL (Winkler et al., 2003) is a space telescope run by the European Space Agency for the observation of gamma rays. It was launched into orbit on October 17 2002 from Baikonur in Kazakhstan by use of a PROTON rocket. Its originally mission length was planned to be three years. Since then the duration of the mission has been extended multiple times, and currently as of 2018, INTEGRAL is still operating. It circulates on a highly eccentric orbit having an altitude of perigee of 9000 km and an altitude of apogee of 154 000 km with a period of 72 h and an inclination of 52.2°. This minimizes INTEGRAL's retention time near Earth and therefore inside the radiation belts. These radiation belts consist of charged particles mostly originating from solar winds or cosmic rays, which are trapped inside the terrestrial magnetic field. They increase the instrument's background rates and can decrease the detector's quality due to radiation damage. Hence, a highly elliptical orbit was chosen. INTEGRAL's goal is the investigation of outer space via gamma rays subsequently to the NASA instrument COMPTON. That covers the exploration of the most violent and energetic phenomena and objects such as black holes, neutron stars, active galactic nuclei, GRBs and supernovae. On the one hand, these objectives are achieved by precise spectroscopy to determine spectral properties, and

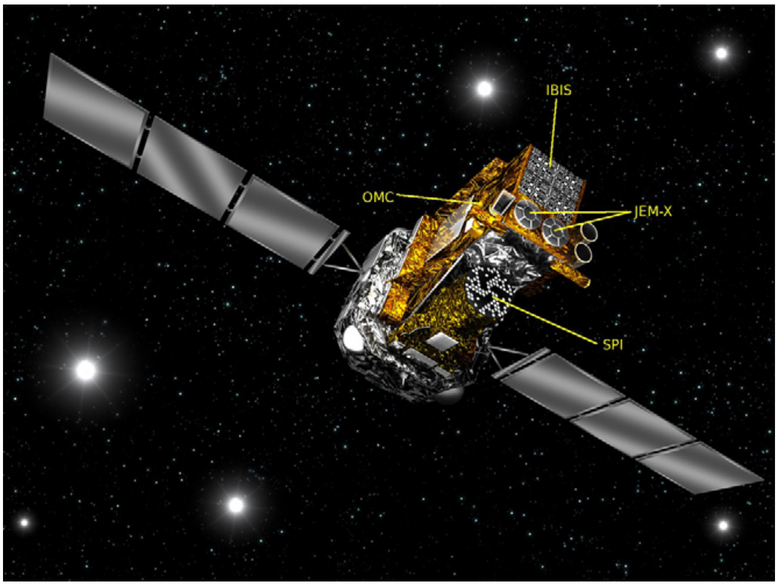

Figure 2.1: Artist impression of INTEGRAL with its instruments labeled; picture from (Diehl, 2013)

on the other hand by accurate imaging to identify and locate gamma ray sources. For that purpose INTEGRAL is equipped with a variety of instruments as seen in Fig. 2.1. First of all, it carries the imager IBIS, which is used for fine imaging in the energy range of 15 keV to 10 MeV. It uses a coded mask to obtain spatial information. Gamma rays cannot be focused by conventional lenses or mirrors. That is why a coded mask, or more specifically, a pattern made of a material opaque to gamma rays, e.g. lead or tungsten, is used to cast a shadow on the detector plane. The location of the gamma ray source can then be reconstructed from the shadow. This method is used for all gamma-ray and X-ray telescopes aboard INTEGRAL. The spectrometer SPI and its anti-coincidence system are described in more detail in the subsequent sections. In addition to the two main instruments, INTEGRAL is equipped with two identical JEM-X units, used for monitoring in the X-ray spectrum, and an Optical Monitor (OMC). The OMC observes the optical emission of INTEGRAL's main targets. Monitoring helps to identify the object and to align the spacecraft properly. All the listed instruments are coaligned on the spacecraft in order to study the same target in different ranges and with different emphases.

2.2 The Spectrometer SPI

The SPectrometer for Integral (Vedrenne et al., 2003) analyzes spectral properties of gamma-ray sources in the range of 20 keV to 8 MeV. It accomplishes a spectral resolution of 2.5 keV at 1.3 MeV and an angular resolution of 2.5° within a FoV of 16° x 16°. SPI with its components can be seen in Fig. 2.2. The camera consists of 19 actively cooled semiconductor detectors made of germanium arranged in a hexagonal array. Due to cosmic-ray interactions irregularities in the atomic lattice of

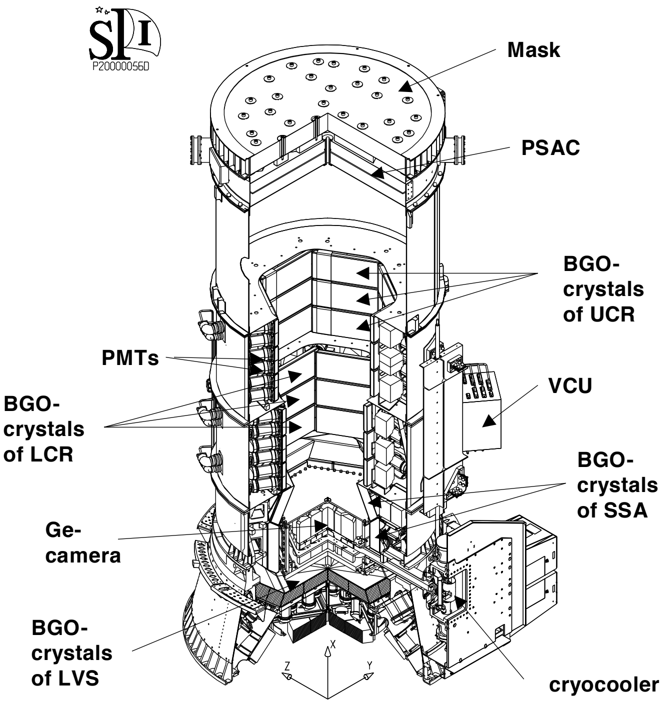

Figure 2.2: The Spectrometer SPI; picture from (von Kienlin et al., 2004)

the Ge detectors can emerge. As a consequence the detector's energy resolution degrades over time. An annealing of the Ge crystals twice a year can restore most of its lost efficiency. Another issue is that the gamma-ray camera also detects incoming photons and particles penetrating the instrument from outside its FoV. This produces a high background that overshadows the desired signal. The background is mostly caused by cosmic-ray particles and cosmic-ray interactions with the spacecraft, leading to nuclear de-excitation gamma rays. In order to protect the camera and suppress these signals, SPI has the ACS

2.3 The Anti-Coincidence Shield, ACS

The main purpose of the ACS (von Kienlin et al., 2004) is to provide a veto signal, so that simultaneous events detected by SPI and the ACS can be rejected, and SPI's background signal can be reduced. For that the ACS needs to be able to detect all kinds of high energy photons and charged particles arriving from outside of SPI's FoV. It consists of 91 scintillation detectors made of bismuth germanate (BGO) crystals, which are arranged in four subunits. These are the lower veto shield (LVS), consisting of 36 crystals, the upper-collimator ring (UCR), the lower-collimator ring (LCR) and the side-shield assembly (SSA), each consisting of 18 crystals. The last three units build the upper veto shield (UVS). The thickness of the crystals ranges from 16 mm to 50 mm resulting in a total mass of 512 kg of all BGO crystals. The detector's arrangement resembles a cylindrical shape, so that the whole spectrometer is covered except its FoV. Directly under the coded mask, a plastic scintillator (PSAC) is attached to reduce the background from positron annihilation photons at 511 keV, which are produced by impacts on the mask's material. Although it is part of the ACS, PSAC is not considered further in this thesis.

2.3.1 GRB Measurements with the ACS

Besides its main function as a veto signal provider for SPI, the ACS can also be used for scientific purposes (Rau et al., 2005). Its large surface (effective area of approximately $0.3\,\mathrm{m}^2$) and its omnidirectional view make it a suitable instrument for GRB detection. The spatial resolution of the ACS is limited by the geometry and size of the BGO units and by the read out procedure. As we shall see later, the main data of the ACS consists of the count rate of all scintillation detectors summed up and the individual detector units are only read out every second. In principle, this gives spatial information for long and bright events, but is restricted for GRBs. This drawback can be bypassed by adding the ACS to the third Interplanetary Network (IPN). The IPN is a group of spacecrafts, all equipped with GRB monitors. If all these instruments detect the same GRB, the location on the sky can be determined via the triangulation method, or in other words, through the comparison of the different arrival times. So, the ACS can contribute to the research of GRBs by gathering data independently or complement the search for specific events.

2.3.2 Scintillation Detectors

The scintillation detectors used in the ACS consist of three parts: a scintillation crystal, viewed by two photomultipliers (PMTs) and a front-end electronic box (FEE).

Scintillators (Knoll, 2000, p. 219-231) are materials that are able to absorb the energy of incoming particles and re-emit the energy in the form of light. There are inorganic and organic materials with that property, but for most applications in high-energy physics, inorganic scintillators, meaning crystals, are preferred. The scintillation mechanism in crystals works due to the electronic band structure. If an incoming high-energy particle hits the crystal, it is able to excite many electrons from the valence band to the conductor band. The higher the energy of the incoming particle, the more electrons get excited. If those excited electrons de-excite back in their ground state, they emit photons. However, these photons are typically outside of the optical spectrum, because the energy gap between the bands is too large and therefore the photons energies are too high. In order to produce photons in the optical spectrum impurities are added to the crystals. These impurities create spots where the band structure is modified in such a way that the energy gap is smaller. If electrons de-excite through these additional energy states they produce visible photons. The left part of Fig. 2.3 shows a sketch of this process. Regarding the ACS, the material of choice is bismuth germanate ($Bi_4Ge_3O_{12}$ or BGO) (Knoll, 2000, p. 239-240). It has a high density ($7.5\ \frac{g}{cm^3}$) and a high atomic number (83), which results in a high absorption efficiency, especially for gamma rays. In contrast to typical inorganic scintillators, BGO is a pure scintillator, which means it does not need impurities. The scintillation mechanism works due to an optical transition of the Bi^{3+} ion. BGO produces about 8000-10000 scintillation photons per MeV deposited energy (Rau et al., 2005). They have an average wavelength of 480 nm, i.e. blue light. In order to detect scintillation photons, PMTs observe the BGO crystals. A PMT, as seen in the right part of Fig. 2.3, is a vacuum tube with a photocathode, several dynodes and an anode in it. Each dynode has a more positive electrical potential than the previous one. So if an incoming photon hits the photocathode, it releases an electron, the primary electron, via the photoelectric effect. The electron gets oriented through a focusing electrode and then accelerated towards the first dynode, gains kinetic energy on its way and is then able to release many more secondary electrons from the dynode. Those electrons travel to the next dynode and the process is repeated many more times until an avalanche of electrons arrives at the anode. This results in a voltage pulse, which can be read out by the electronics. The height of the voltage pulse rises with the number of primary electrons and therefore with the number of scintillation photons. Moreover, the detection efficiency, i.e. the probability to detect a signal, is dependent on the particle energy. The

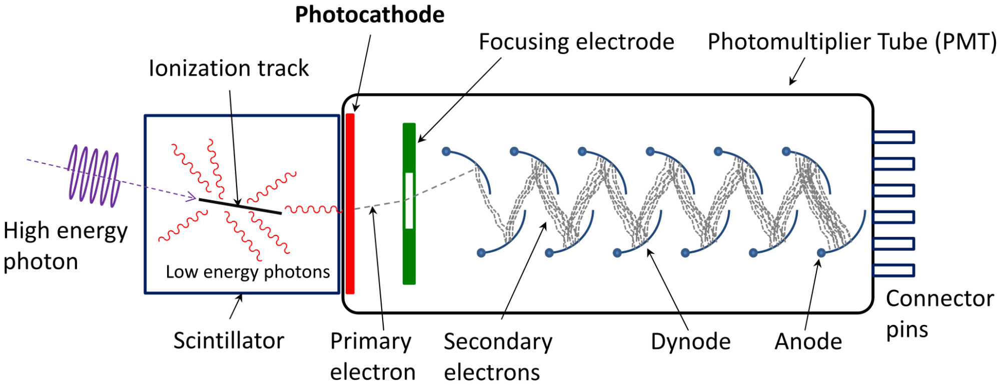

Figure 2.3: Schematic of a scintillator coupled to a PMT[1]

---

[1] picture from wikimedia.org/wikipedia/commons/e/e8/PhotoMultiplierTubeAndScintillator.svg [last visit 14.11.18]

efficiency can be influenced by different criteria. Some of these are the crystal's shape, the placement of the PMT or the type of incoming particle. This behavior will be described by a response function later on in Section 3.3.2.

The last component in this chain is a FEE (von Kienlin et al., 2004) to read out the signal. The FEE registers a count if the energy of the detected particle is above a certain energy threshold. The electronics allow 32 discrete settings, each corresponding to a certain threshold. The arrangement of all those components on the ACS can be seen in Fig. 2.4. Each BGO crystal is coupled with two PMTs. In addition, each FEE reads out the summed up signal of two PMTs viewing different BGO crystals. This setup ensures that if a single PMT or FEE fails the BGO crystal is still monitored.

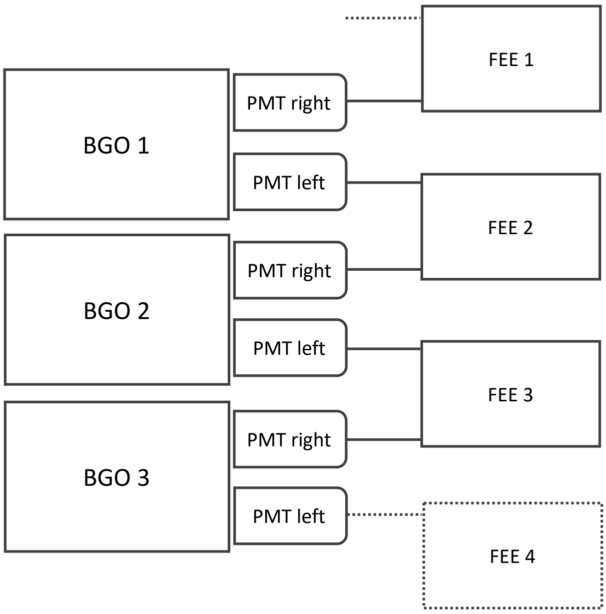

Figure 2.4: Sketch of the setup used in the ACS

2.3.3 Calibration of the Energy Threshold

In order to set an energy threshold, one needs to know which FEE setting corresponds to which energy level. For that purpose, a calibration with two known gamma-ray sources was performed on Earth (Attié et al., 2003). The isotopes ^{203}Hg with a characteristic line at 297 keV and ^{137}Cs at 662 keV were used. The sources were placed close to the BGO detectors and the count rate for each setting was measured. As a consequence, the setting, corresponding to the threshold energy nearest to the characteristic gamma-ray line of the source, could be determined. The relation between setting and threshold energy was assumed to be linear. Two radioactive sources give two value pairs, which define the linear function. The result is a calibration function for the threshold energy for one FEE. This procedure was performed for each of the 91 FEEs. With this calibration a desired threshold energy can be set. However it needs to be remarked that the set threshold is not entirely sharp. Because of the cross-strapping setup (Fig. 2.4), the FEEs read out the summed up signal of two PMTs. The PMTs and BGO crystals can have differences in their properties, such as the crystals thickness or the light yield of two crystals could be different for the same energy. This broadens the threshold and the

set value only roughly matches the desired value.
After the calibration process, a threshold value of around 75 keV (75^{+50}_{-25} keV) (Jean et al., 2003) was set for all FEEs. The issue is that during many years of observation in space, things could have changed. There are many factors that could have had an influence on the detector's properties, e.g. exposure to cosmic rays, decline of the BGO crystal's efficiency, a variation in temperature or a degradation of the electronics. As a result, the original calibration could lose accuracy and it would be helpful to know if there are changes, and if possible to perform a calibration with the capabilities available for INTEGRAL in space.

3. ACS Data

3.1 Data Structure

As already mentioned, the only spectral information is a lower energy limit. So every time the detector produces a count, a photon or charged particle with a higher energy than the threshold value has passed the detector. Therefore, all of the ACS data (Rau et al., 2005) exists in the form of detected counts over a certain time interval. During INTEGRAL's entire observation time two kinds of data packets are measured with the same threshold of about 75 keV. A packet describes a data set produced with a specific readout procedure. The first packet contains the total event rate of all FEEs summed up and is gathered every 50 ms. This provides a continuous light curve. Another packet covers the event rate over 1 s of each individual FEE and is read out every 96 s.

In this thesis additional calibration data of the ACS is going to be analyzed. During the annealings of SPI's Ge detectors every half a year, calibration data for the ACS is gathered. For that purpose, every FEE records the cumulative count rate over 5 s of each of the 32 threshold settings. Two FEEs are broken, so there are 89 FEEs left recording. This run across all settings is called a loop. During one of these calibration periods, about 50 loops are performed on average, but the exact number can vary from around 20 to 300.

3.2 Background Radiation and High-Energy Gamma-Ray Sources

For the original calibration on Earth, a well known source was used. In space on the other hand it is impossible to obtain an isolated signal from a known source. Therefore it is important to understand the emergence of the data. The measured particles can have vastly different origins. Depending on their origin different models need to be used to describe the data. The sources responsible for the overall majority of the ACS data are pictured below.

3.2.1 Cosmic Rays

Cosmic rays (De Angelis and Pimenta, 2015, Chapter 1.4) are high-energy particles. They can originate from the sun, inside our Galaxy or have an extragalactic origin. Cosmic rays mostly consist of massive particles. The bulk of cosmic rays (around 88 %) are protons, i.e. hydrogen nuclei, and about 10 % are alpha particles, i.e. helium nuclei. Approximately 1 % account for nuclei of heavier elements. So together about 99 % are atomic nuclei and the remaining 1 % are electrons and photons. A small fraction is composed of stable antimatter particles and neutrinos. The measured energy spectrum of cosmic rays can be seen in Fig. 3.1. In the figure the flux (number of incident particles per unit energy, per second, per unit area, and per unit solid angle) is plotted as a function of energy. The graphic is divided in three parts which represent the main origin of particles in this energy range. The yellow region marks the energy region in which the particle emission of the sun is dominant. The light blue region indicates a predominant origin within the Galaxy and the purple one represents extragalactic origin. Most of the counts, measured by the ACS, are produced by particles with energies between 50 keV and 10 MeV. Hence solar cosmic rays are the biggest influence on the ACS data.

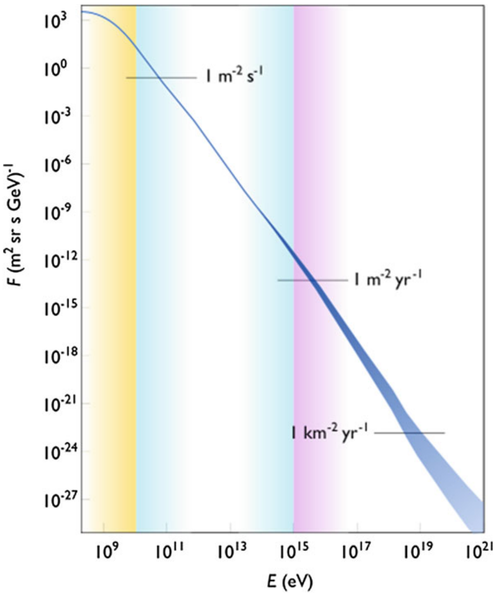

Figure 3.1: Cosmic-ray spectrum; picture from (De Angelis and Pimenta, 2015)

The cosmic-ray spectrum follows approximately a power law distribution (described in more detail in 3.3.1), which means that a higher energy of the particle corresponds to a lower flux. The exact values of the flux in Fig. 3.1 just serve as an example and do not represent the values measured with INTEGRAL. Depending on where and when the cosmic-ray spectrum was recorded, the exact shape and intensity of the power law can vary. Solar phenomena, for instance, can have a huge influence on the intensity of cosmic rays with low energy. A phenomenon worth mentioning here is the solar cycle. The solar cycle (Balogh et al., 2014) is a periodic change in the suns activity. One cycle has an average length of 11 years and plays a role in most models that describe solar phenomena. As a consequence for the ACS, a modulation of the flux intensities of cosmic rays is seen. During phases of high solar activity, the presence of magnetic fields makes it harder for cosmic rays to reach Earth's proximity. So an increase in solar activity implies a decrease in the cosmic ray spectrum's intensity. The solar cycle is visible in the ACS data, since it evaluates data from a time period of 16 years.

3.2.2 Solar Flares

Solar flares are flashes of increased brightness on the suns surface caused by reconnection events of magnetic field lines (Sturrock et al., 2001). These reconnection events can set up environments for particle acceleration towards deeper layers of the sun and result in the emission of radiation across the electromagnetic spectrum. Bremsstrahlung and nuclear excitations are responsible for radiation in the X-ray and gamma-ray spectrum. Solar flares are often accompanied by coronal mass ejections, i.e. the release of plasma from the solar corona. An example for a very intense and bright solar flare is the 2003 October 28 solar flare (Gros et al., 2004). A bright flash of X-rays and gamma rays were observed starting at around 11:02 a.m. and lasting for about 15 minutes. After around 11:20 a.m. particles were detected, showing the time delay between gamma-ray and particle emission. The flare was detected by several instruments on board of INTEGRAL, including the ACS. The total count rate of all BGO detectors summed up during the time of the solar flare can be seen in Fig. 3.2. The dotted blue line indicates the mean count rate of the background. This event serves as an example for how a solar flare appears in the ACS data.

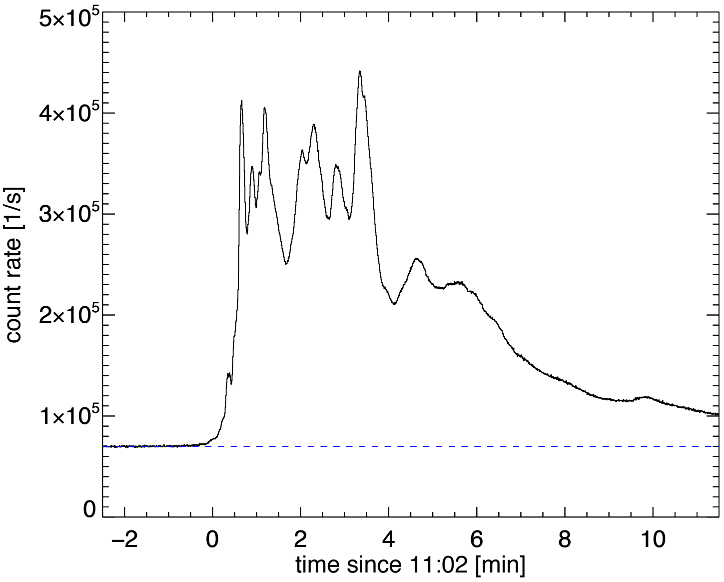

Figure 3.2: ACS count rate during a solar flare detected on October 28 2003

3.2.3 Gamma-ray bursts

The ACS can be used for GRB measurements (Rau et al., 2005) due to its large surface and omnidirectional view. GRB light curves can vary widely in their properties such as duration, intensity, number of peaks and also the spectrum might change from burst to burst, which makes their study a challenging field of research. However, progress has been made and thanks to previous missions like NASA's Compton Gamma Ray Observatory with its BATSE detectors, extensive catalogues of GRBs were acquired. Despite the huge GRB diversity, a bimodality in duration has been observed. This way GRBs can be classified into two groups (Vedrenne and Atteia, 2009, Chapter 1). The first group contains short GRBs, which account for about 30 % and have a typical duration of less than two seconds. They also show a higher peak energy in their spectrum compared to the second group, long GRBs, with a duration of more than two seconds and a fraction of 70 %. Due to their different observable properties, short and long GRBs are thought to originate in different events. The favored model for the origin of short GRBs is a merger event of two compact objects with at least one neutron star involved. These events are thought to produce kilonovae and result in the emission of short GRBs. This model was confirmed by the detection of GRB170817A (Abbott et al., 2017). On the other hand, long GRBs are assumed to emerge in core-collapse supernovae, which occur at the latest stage in the evolution of massive stars.

The ACS cannot provide insights in the distribution of spectra, but can contribute searches for specific events or expanding GRB catalogues, and therefore investigate the distribution of duration and intensity. To display the diversity of GRBs and what their light curves can look like, two examples are given below. Fig. 3.3 shows the light curve of a bright and short GRB from December 12, 2003.

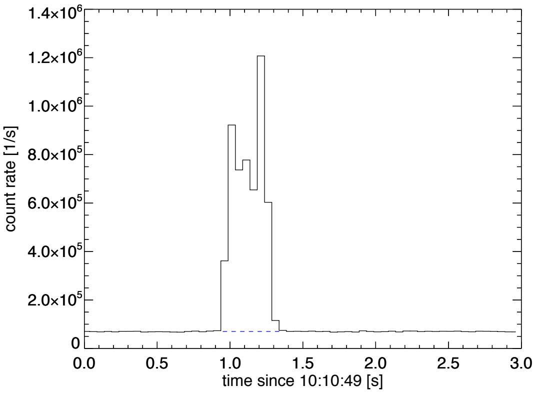

Figure 3.3: Bright short GRB 031214

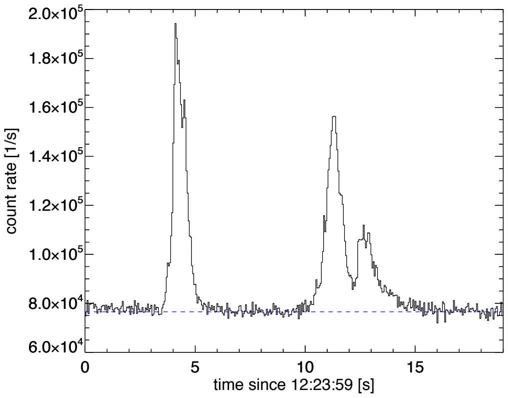

Figure 3.4: Triple-peaked GRB 040302

The signal is binned in 50 ms time intervals. The dotted blue line indicates the mean count rate of the background. Fig. 3.4 displays a GRB with three peaks from March 2, 2004. The short GRB shows a much higher peak intensity and a shorter duration of less than one second compared to the individual peaks of GRB 040302.

Solar flares and GRBs will be of no relevance for the later data analysis because of their short duration and therefore their little influence on the data set as a whole. The only considered data source is going to be cosmic rays.

3.3 The ACS Calibration Data

3.3.1 Characterizing the Calibration Data

In the subsequent sections, the calibration data of the ACS will be described. This includes examples of what the actual data sets typically look like and a detailed description of how the data and its emergence can be modeled. As already mentioned the ACS calibration data is gathered during the annealings of SPI's Ge detectors every half a year. An example data set of such calibration period is presented for revolution 1916 (INTEGRAL's data sets are classified into revolutions, meaning the number of orbits, in which the data was collected. One revolution covers a time period of 72 hours). Data from other revolutions follow the same structure and have similar shapes.

The total event rate of all FEEs summed up during a section of such a calibration period can be seen in Fig. 3.5. It shows that about every ten minutes a loop is performed. The image shows three of them, but the process is repeated about 50 times on average. Additionally, the data of every individual

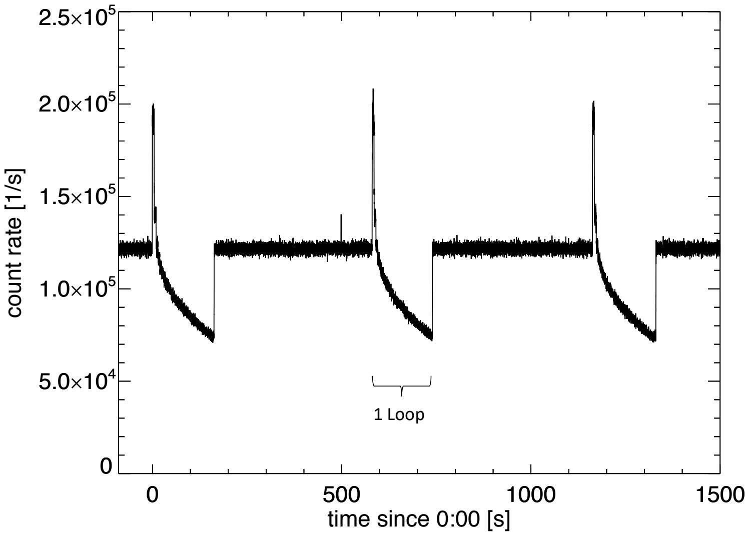

Figure 3.5: Total count rate gathered during revolution 1916 at 12 pm on February 6 2018

FEE is gathered during each loop. Fig. 3.6 shows the data collected during the first loop of FEE 85. The data contains the counts measured for each of the 32 possible settings over a period of 5 seconds. With an increase of the setting number the counts decrease, because a higher setting corresponds to a higher energy threshold of the detector and therefore less counts are measured. The uncertainties of the counts resemble the square root of their value, since the count data is Poisson distributed around their expectation value (see also section 3.4). In order to visualize how the data can vary among the

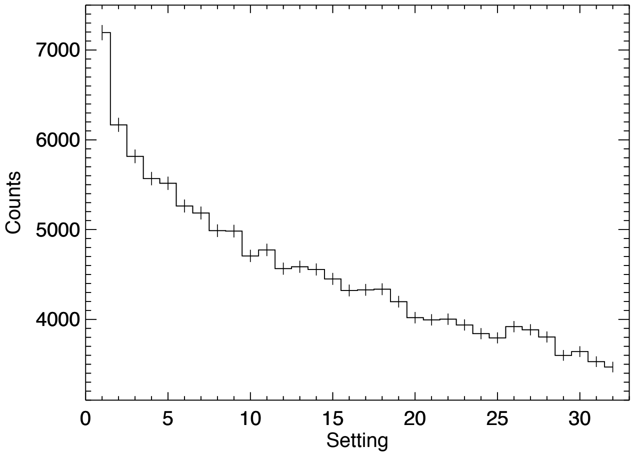

Figure 3.6: Counts for each setting of FEE 85 measured during the first loop of revolution 1916

FEEs, Fig. 3.7 contains counts for each of the settings for every one of the 91 FEEs. The x-axis displays the setting number and the hidden y-axis the number of FEE. The general curve shape is similar among the FEEs, but the intensity varies strongly. This variation can be explained by the fact that the crystals have different shapes and are exposed differently to cosmic rays depending on their position and orientation on the spacecraft. FEE 57 and FEE 82 are broken and therefore produce no counts.

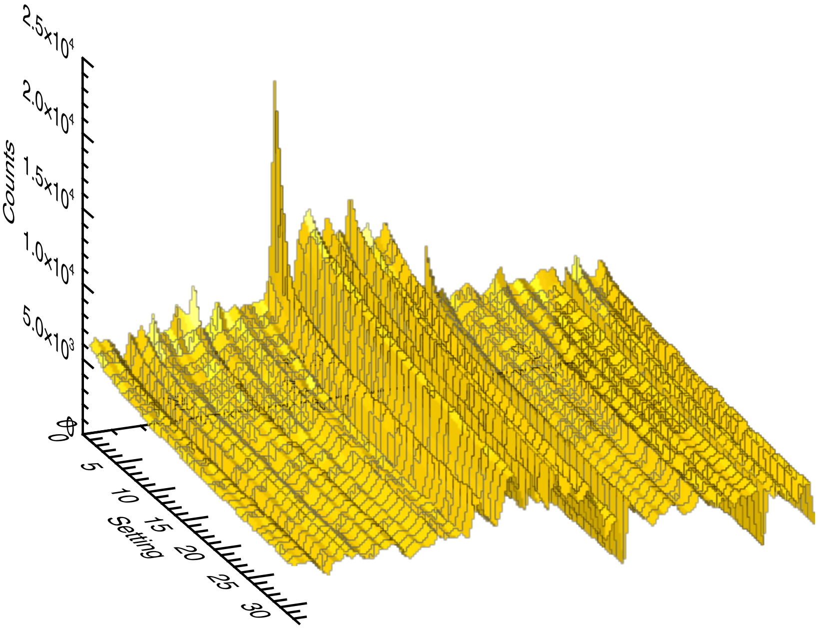

Figure 3.7: Counts for each setting for all FEEs during the first loop 1 of revolution 1916

3.3.2 Modeling the Data

In order to register changes in the performance of the BGO detectors, one needs to understand how a single data set emerges and how this process can be parameterized. This results in a model, which is then fitted to the data.

The first step towards such a model is an assumption about the major data sources. The dominant source of ACS events are cosmic rays in the energy range of approximately 50 keV − 10 MeV. The spectrum of cosmic rays $F(E)$ can be approximated by a power-law distribution:

$$F(E) = A \cdot E^{\alpha} \tag{3.1}$$

This power law has two parameters, the intensity A and the index α. Based on the inclined shape of the spectrum, α has a negative value. The general shape of $F(E)$ can be seen in Fig. 3.8. Consequently for the main fitting model it is assumed that the BGO detectors are exposed to a power-law shaped spectrum of cosmic rays. Next the response function of BGO detectors needs to be factored in (Knoll, 2000, p. 236). Scintillation detectors have an efficiency depending on the energy of the incoming particle. The efficiency is the ratio between the number of detected particles and the number of particles actually striking the detector. This resembles the probability for the detection of a single particle with energy E, and can be described with a response function $\mu(E)$. Therefore the codomain of the response function needs to be higher than 0 and less than 1. It also needs to contain low detection probabilities for small energies and a smooth continuous transition towards higher probabilities for higher energies. An actual response function of a BGO detector would decrease again after a certain energy value. However considering the energy range, in which the ACS receives most of its counts, this behavior can be neglected. In order to meet all of the above criteria such a response function can

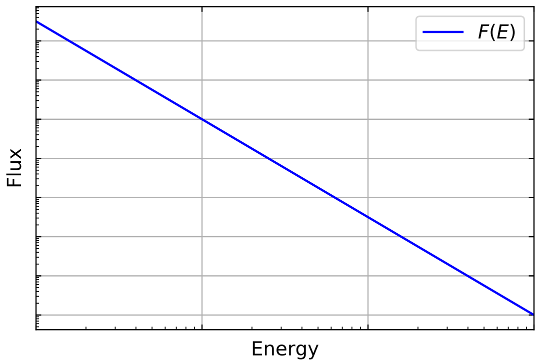

Figure 3.8: Power law as an approximation for the cosmic-ray spectrum

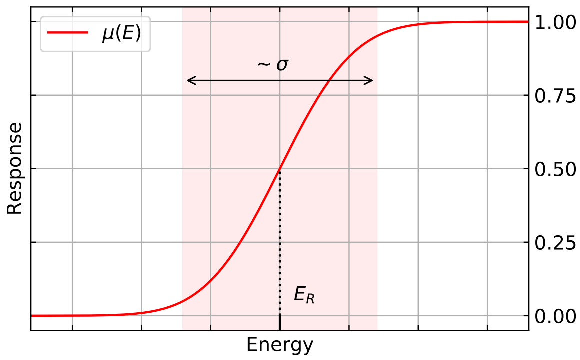

Figure 3.9: Model function to account for the response of the BGO detectors

be modeled by a modified error function:

$$\mu(E) = 0.5 \cdot \left[\operatorname{erf}\left(\frac{E - E_R}{\sigma\sqrt{2}} \right) + 1 \right] \tag{3.2}$$

A conventional error function has a codomain between -1 and 1 and crosses the x-axis in the point of origin. The conventional error function is defined as:

$$\operatorname{erf}(x) = \frac{2}{\sqrt{\pi}} \int_0^x e^{-\tau^2} \mathrm{d}\tau \tag{3.3}$$

To obtain the desired response function, the error function is shifted by 1 in the y-direction, scaled by a factor of 0.5 and then parameterized by E_R and σ. E_R provides the shift in energy-direction and marks the energy value with a detection probability of 0.5. The width and the slope of the transition area is determined by σ. The greater σ is, the smaller is the slope. An illustration of Function (3.2) can be seen in Fig. 3.9. the actual spectrum, therefore, registered by the detectors needs to take the response function into account. It can be expressed by the combined function: $F(E) \cdot \mu(E)$, in which the spectrum is weighted with the associated detection probability.
As aforementioned the BGO detectors allow to set a threshold energy. In the following, this threshold value will be called E_{min}. If one FEE detects a certain amount of counts C in a given time period, the counts resemble the integral over the combined spectrum function from the energy threshold up to infinity:

$$C(E_{min}) = \int_{E_{min}}^{\infty} F(E) \cdot \mu(E) \, \mathrm{d}E \tag{3.4}$$

In reality the lower integral boundary is not completely sharp. The energy threshold has an uncertainty, meaning there is a certain probability for particles with lower energies to be detected and for higher energies to be missed. As an approximation this behavior is ignored and the threshold is viewed as sharp. Fig. 3.10 shows a sketch of the combined function with the area enclosed by it and E_{min} shaded, which equals Eq. (3.4). The threshold energy E_{min} is determined through the setting s. The FEEs offer 32 discrete settings but for the model fitting, s is going to be treated as a continuous physical parameter. A linear relation, analogous to the Earth calibration, is assumed for the relation

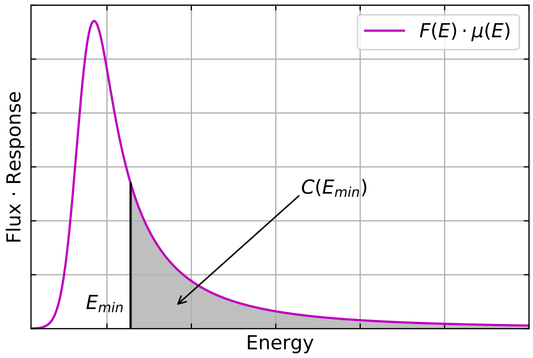

Figure 3.10: Combined function integrated from the threshold energy

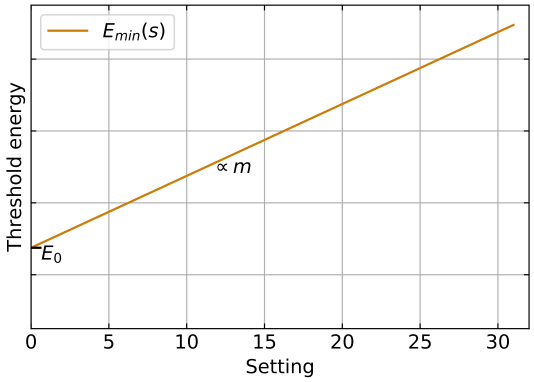

Figure 3.11: Linear relation between threshold energy and setting

between threshold energy and setting, as seen in Fig. 3.11:

$$E_{min}(s) = E_0 + m \cdot s \tag{3.5}$$

It is defined by E_0, which indicates the threshold value at the setting $s = 0$, and by the slope m, which determines how strongly the threshold value rises with an increase in setting number. Inserting this relation into Eq. (3.4) results in an expression for counts as a function of setting:

$$C(s) = \int_{E_0+m\cdot s}^{\infty} F(E) \cdot \mu(E)\,\mathrm{d}E \tag{3.6}$$

Finally the cosmic-ray spectrum and the modified error function for the response function are inserted. The equation describes a relation between counts and setting as displayed by the data and contains six free parameters. The final model which will be fitted to the data is expressed in integral form:

$$C(s; A, \alpha, E_R, \sigma, E_0, m) = 0.5A \int_{E_0+m\cdot s}^{\infty} E^{\alpha} \cdot \left[\mathrm{erf}\left(\frac{E - E_R}{\sigma\sqrt{2}}\right) + 1\right] \mathrm{d}E \tag{3.7}$$

The integral has no analytic solution and needs to be integrated numerically. An example step function of Eq. (3.7) for 32 setting values is shown in 3.12. The differential counts $\Delta C(s)$ can be determined by taking the difference between the counts for setting s_i and the counts for setting s_{i+1}. This resembles the area enclosed by the combined function $F(E) \cdot \mu(E)$ and the two threshold values. The function of the differential counts is therefore proportional to the combined function. Its general shape is displayed in Fig. 3.13.

3.4 Comparing Fitting Methods

The general goal of curve fitting is to find a model that explains the data best, meaning a function that has the best fit to a set of data points. The model function contains free parameters and the fitting process aims to find the best values for those parameters. There a two common approaches (Hauschild and Jentschel, 2001): The maximum likelihood estimation (MLE) and the method of least

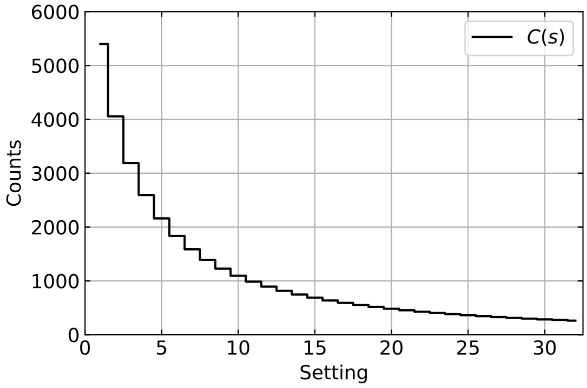

Figure 3.12: Counts as a function of setting

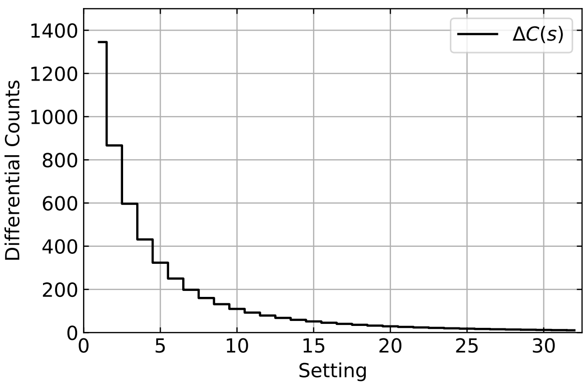

Figure 3.13: Differential counts as a function of setting

squares, which is a special case of the MLE, see Sec. 3.4.2. In the following, the two methods will be briefly portrayed and it will be explained with the aid of an example why the method of least squares is used for the later data analysis.

3.4.1 Maximum Likelihood Estimation

In general, the MLE tries to maximize the probability that the data has occurred given an expected model defined by a set of parameters. The model with the highest probability should then be favored. In order to fulfill this approach, the MLE uses a likelihood function L, which is determined by the measurement process. L expresses the likelihood that the measured data points arose from the model and its parameters. This is the quantity that should be maximized. Before this likelihood function can be formulated, one needs to know the probability for the emergence of a single data point.
In that regard, let d_i be a data point out of a data set. The model provides an expectation value $f(x_i;\vec{\Theta})$, which depends on a set of parameters $\vec{\Theta}$, for that data point. The data examined in this thesis resembles counts and thus follow a Poisson distribution. That means that the probability for the emergence of a single data point is given by:

$$P_P(d_i; f(x_i;\vec{\Theta})) = \frac{(f(x_i;\vec{\Theta}))^{d_i}}{d_i!} e^{-f(x_i;\vec{\Theta})} \tag{3.8}$$

The likelihood function includes the probability of every data point in order to obtain an overall probability for the arising of the data set:

$$L(\vec{\Theta}) = \prod_i P_P(d_i; f(x_i;\vec{\Theta})) = \prod_i \frac{(f(x_i;\vec{\Theta}))^{d_i}}{d_i!}\, e^{-f(x_i;\vec{\Theta})} \tag{3.9}$$

This expression is only dependent on the parameters $\vec{\Theta}$ and needs to be maximized towards them. Instead of maximizing L, it is mathematically more convenient to use the logarithm of L:

$$-2\ln L(\vec{\Theta}) = 2\sum_i \Big(f(x_i;\vec{\Theta}) - d_i \ln(f(x_i;\vec{\Theta}))\Big) + const \tag{3.10}$$

Minimzing the negative logarithm of L results in the same parameters as maximizing L, because the logarithm is a strictly monotonic function. Finally the parameters are obtained by finding the zero of the first derivative:

$$\frac{\mathrm{d}\ln L}{\mathrm{d}\vec{\Theta}} = 0 \tag{3.11}$$

In order to find the zero for more complex terms, a minimization algorithm like the Levenberg–Marquardt algorithm can be used.
This is the correct strategy for fitting Poisson-distributed data. When the data follows a normal distribution, the resulting approach is called method of least squares, and is explained below.

3.4.2 Method of Least Squares

Geometrically, the method of least squares tries to minimize the absolute distances between model and data points in such a way, that the model and the data match in the best possible way. This becomes apparent when derived by following a similar procedure as before. The difference now is that a normal distribution for the data is used. This means the probability to measure a single data point is given by:

$$P_N(d_i; f(x_i; \vec{\Theta}), \sigma_i) = \frac{1}{\sqrt{2\pi\sigma_i^2}} \exp\left(-\frac{(d_i - f(x_i; \vec{\Theta}))^2}{2\sigma_i^2}\right) \tag{3.12}$$

Here σ_i indicates the measurement uncertainties of d_i. The likelihood function now equals:

$$L(\vec{\Theta}) = \prod_i P_N(d_i; f(x_i; \vec{\Theta})) = \prod_i \frac{1}{\sqrt{2\pi\sigma_i^2}} \exp\left(-\frac{(d_i - f(x_i; \vec{\Theta}))^2}{2\sigma_i^2}\right) \tag{3.13}$$

Calculating the negative logarithm of L gives:

$$-2\ln L(\vec{\Theta}) = \sum_i \left[\frac{\left(d_i - f(x_i; \vec{\Theta})\right)^2}{\sigma_i^2} + \ln\sigma_i^2 + \ln(2\pi)\right] \tag{3.14}$$

If σ_i is known, which is the case in the context of this thesis, σ_i does not depend on $\vec{\Theta}$. It therefore has no influence on the minimization. The term to be minimized then equals:

$$-2\ln L(\vec{\Theta}) = \sum_i \frac{\left(d_i - f(x_i; \vec{\Theta})\right)^2}{\sigma_i^2} + const \tag{3.15}$$

The resulting function sums up the squared residuals weighted by the squared measurement uncertainties. A residual is the difference between the observed value and the value provided by the model. This function is called χ^2:

$$\chi^2(\vec{\Theta}) = \sum_i \frac{\left(d_i - f(x_i; \vec{\Theta})\right)^2}{\sigma_i^2} \tag{3.16}$$

The parameters are now again obtained by finding the zero of the derivative:

$$\frac{\mathrm{d}\,\chi^2}{\mathrm{d}\vec{\Theta}} = 0 \tag{3.17}$$

3.4.3 Estimating the Confidence Limits

The confidence limits of the parameters are estimated by investigating the likelihood function at the best fit values (Blobel and Lohrmann, 1998, Chapter 6.4). For high values of d_i, its shape approximates a gaussian function. The 1σ region of that function defines the the confidence limit at that significance. So the goal is to find the parameter values that contour this region. The MLE uses the logarithm of the likelihood function, which has a parabolic shape. The mentioned 1σ realm is now defined by the values where -2ln$L$ changes by 1. For more than one parameter this interval is different. In the case of two parameters -2ln$L$ needs to change by 2.3 and by 3.5 for three parameters. The 1σ confidence limit of the parameters therefore are determined by the boundaries at:

$$-2\ln L(\vec{\Theta}_c) = -2\ln L_0 + 1 \qquad \text{for 1 parameter} \tag{3.18}$$

$$-2\ln L(\vec{\Theta}_c) = -2\ln L_0 + 2.3 \qquad \text{for 2 parameters} \tag{3.19}$$

$$\vdots$$

L_0 is the maximum likelihood at the best parameters $\vec{\Theta}_0$. The confidence limit is therefore given by $\vec{\sigma}_\Theta = \vec{\Theta}_c - \vec{\Theta}_0$. The same goes for parameters, which were determined by the method of least squares. Since the relation,

$$\chi^2 = -2\ln L, \tag{3.20}$$

applies, the estimation of confidence limits works analogous.

If the data is normal distributed, the method of least squares is the fitting method of choice. However as already mentioned the data examined in this thesis resembles counts, which follow a Poisson distribution. So, strictly speaking, the method of least squares does not apply, and the maximum likelihood estimation for Poisson-distributed data would be the correct method.

3.4.4 Comparative Example

Although it seems like it is the incorrect approach, the method of least squares will be used in the later data analysis. The reason why this is valid, is that the count values in the data are very high. A Poisson distribution is asymmetrical and differs strongly from a normal distribution for low values of d_i. But as d_i rises, the Poisson distribution approaches a normal distribution and for sufficiently large values (say $d_i \gtrsim 30$), a normal distribution with a standard deviation of $\sqrt{f_i}$ is a very precise approximation of a Poisson distribution:

$$P_P(d_i; f_i) \approx P_N(d_i, f_i, \sigma_i^2 = f_i) \qquad \text{for } d_i \gtrsim 30 \tag{3.21}$$

All of the ACS calibration data contains counts in the range of about 1000 to 10000. Hence, the method of least squares can be used unproblematically.

To verify that this assumption holds holds, both methods are applied to an exemplary data set. The counts of a calibrational run from a single FEE from Section 3.3.1 (FEE 85, Loop 1, Revolution 1916) is fitted with an empirical model. The model only contains two parameters and has no physical relevance. It acts as a tool for comparison:

$$f(x; a, b) = 10^4 \cdot (b + x)^{-a} \tag{3.22}$$

The data set with the resulting graphs of the fit and th associated residuals can be seen in Fig. 3.14. Both graphs align well with the data and result in similar χ^2 values ($\chi^2_{LS} = 83.82, \chi^2_{MLE} = 83.57$).

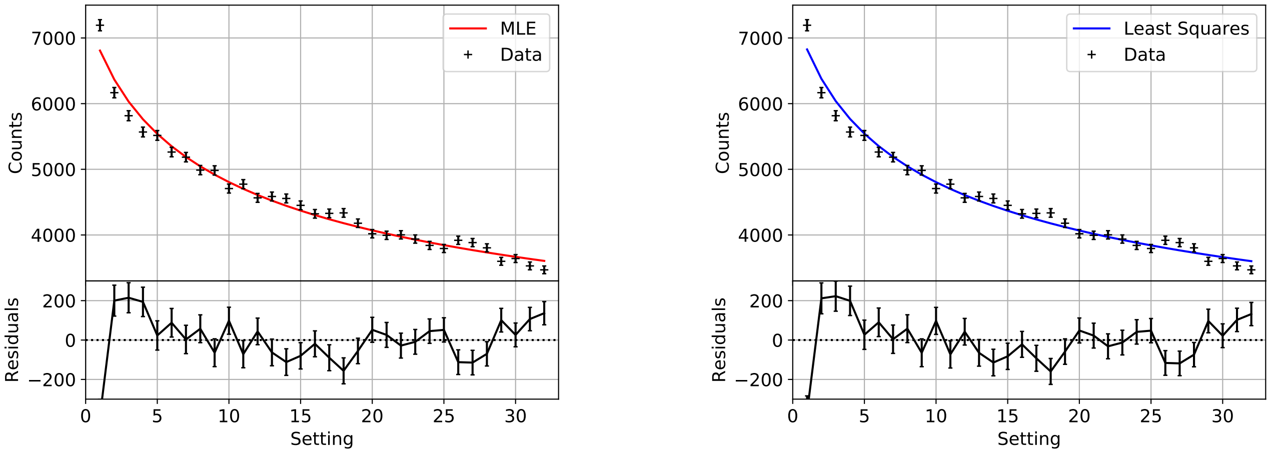

(a) Maximum likelihood estimation **(b)** Method of least squares

Figure 3.14: Data from FEE 85, loop 1, revolution 1916 fitted with both methods

Their associated parameters can be seen in Table 3.1. As expected, both methods result in the same parameters and their differences become negligible at such high counts. Besides, the method of least squares has the advantages over the MLE, that the calculation of the parameters and its confidence limits is mathematically more straightforward and therefore faster to compute. Hence the method of least squares is going to be applied in the data analysis in chapter 4. Rau et al. (2004) states that the ACS data has a measured deviation from a pure Poisson distribution and 1σ corresponds to $1.6\sqrt{C}$. For the analysis the corrective factor of 1.6 is incorporated.

Table 3.1: Resulting parameters of both fitting methods

Param.	MLE	Least Squares
a	0.287 ± 0.003	0.288 ± 0.001
b	3.81 ± 0.09	3.78 ± 0.03

4. Data Analysis

4.1 Characterizing the Model Function

4.1.1 Numerical Integration

The final model, Eq. (3.7), which is fitted to the data, resembles counts as a function of setting and is expressed by a non-analytic integral [1]. In the fit, it is calculated numerically for every setting, by stepwise integration of the energy from a minimum energy to a maximum energy. Strictly speaking, the correct upper integration limit would be infinity, but the spectrum decreases enough at values around 10 MeV - 100 MeV that the difference becomes irrelevant.

The integration is performed by dividing the domain in small intervals and then summing up the resulting columns under the curve. The smaller the intervals the more exact is the integration, but the more time-consuming is the fitting process. The numerical integration is performed from 1 keV to 100 MeV in logarithmic intervals. About 1000 steps provide accurate results.

4.1.2 Parameter Correlations

Before the fitting method is applied to the whole data set, it is tested with individual data examples. By sampling a large grid of the parameters, correlations and a potential degeneracy of the fit is investigated.

The model used for data fitting contains six free parameters. The fitting algorithm aims to minimize χ^2 and outputs the set of parameters at that minimum. The problem of degeneracy appears if the minimum is very shallow or there is more than one minimum in the χ^2-space. Then, the fitting process can result in more than one set of parameters. One possible solution to this would be to combine or rather merge parameters in order to find a way to parameterize the same type of function with less variables. This is not possible in the case of the fitting function (3.7), because there is no analytic solution of the integral and a merger or a reduction of parameters would diminish their physical information. All six parameters represent a property of the detector, the electronics or the incoming spectrum. If the number of parameters is reduced, the individual information is lost, which would make the goal of this thesis unaccomplishable. The model therefore needs to contain all these six parameters.

In order to investigate a potential degeneracy of the fit, a grid method is used. Given an example data set, $\chi^2(\vec{\Theta})$ represents a function depending on the parameters $\vec{\Theta} = [A, \alpha, E_R, \sigma, E_0, m]$. χ^2 therefore

---

[1] Even if the error function is replaced by alternatives that could be parameterized similarly (e.g. logistic function, arctangent function, ...), the result has no analytic solution

represents a function in a 6D-space, which is generated by the parameters. The goal of the grid method is now to sample this function by calculating equidistant points. This is done by using arrays of discrete values for the parameters instead of a continuous range:

$$
\begin{aligned}
A &\in [A_1, A_2, ..., A_N] \\
\alpha &\in [\alpha_1, \alpha_2, ..., \alpha_N] \\
E_R &\in [E_{R,1}, E_{R,2}, ..., E_{R,N}] \\
\sigma &\in [\sigma_1, \sigma_2, ..., \sigma_N] \\
E_0 &\in [E_{0,1}, E_{0,2}, ..., E_{0,N}] \\
m &\in [m_1, m_2, ..., m_N]
\end{aligned}
$$

The values of the arrays cover a big section to include the aspired peaks. The number of used elements N of the parameter arrays is 15 elements. A higher number of elements would result in a too long computational run time. The χ^2 value of every possible parameter combination can then be calculated, which samples the χ^2 function with 15^6 points:

$$\chi^2_{g,h,i,j,k,l} = \chi^2\left(A_g, \alpha_h, E_{R,i}, \sigma_j, E_{0,k}, m_l\right) \tag{4.1}$$

As stated earlier in 3.4.2, for normal distributed data the logarithm equals:

$$-2\ln L = \chi^2 + const \tag{4.2}$$

Hence the following relation applies for the likelihood:

$$L(\vec{\Theta}) \propto e^{-\frac{\chi^2(\vec{\Theta})}{2}} \tag{4.3}$$

Since L expresses a probability for the arising of the data given a certain model, the integral over the whole parameter space needs to equal 1 and the integral of the exponential of χ^2 needs to equal some constant C:

$$1 \overset{!}{=} \int L(\vec{\Theta})\,\mathrm{d}\vec{\Theta} \qquad \Rightarrow \qquad C = \int e^{-\frac{\chi^2(\vec{\Theta})}{2}}\,\mathrm{d}\vec{\Theta} \tag{4.4}$$

Then the likelihood as a function of a single parameter can be expressed by integrating over all other parameters. This represents a probability P for the data occurrence given the associated parameter value. If the parameters of the model, $\vec{\Theta} = [A, \alpha, E_R, \sigma, E_0, m]$, are used, the probability as a function of A, for example, equals:

$$P(A) = \int\!\!\int\!\!\int\!\!\int\!\!\int \frac{1}{C}\,e^{-\frac{\chi^2(\vec{\Theta})}{2}}\,\mathrm{d}\alpha\,\mathrm{d}E_R\,\mathrm{d}\sigma\,\mathrm{d}E_0\,\mathrm{d}m \tag{4.5}$$

If the model parameters are uncorrelated, the resulting distribution for P has the shape of a unique peak at the optimal parameter value. Using the sampled χ^2 function, these probabilities can be calculated by substituting the integrals in Eq. (4.5) with discrete summations.

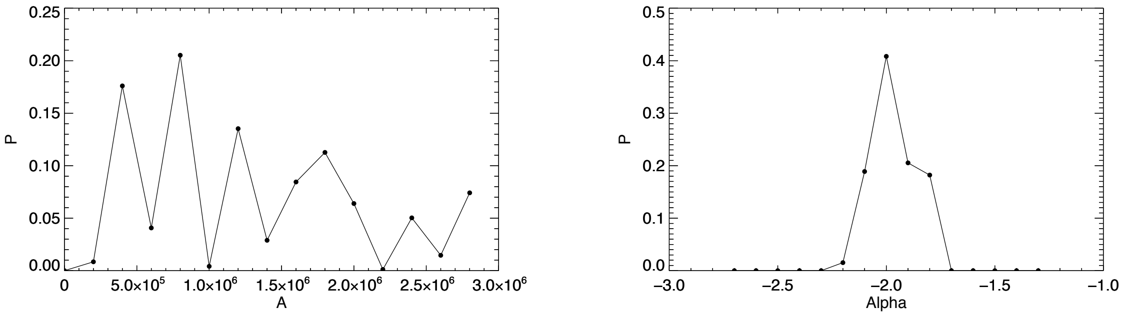

(a) $P(A)$ **(b)** $P(\alpha)$

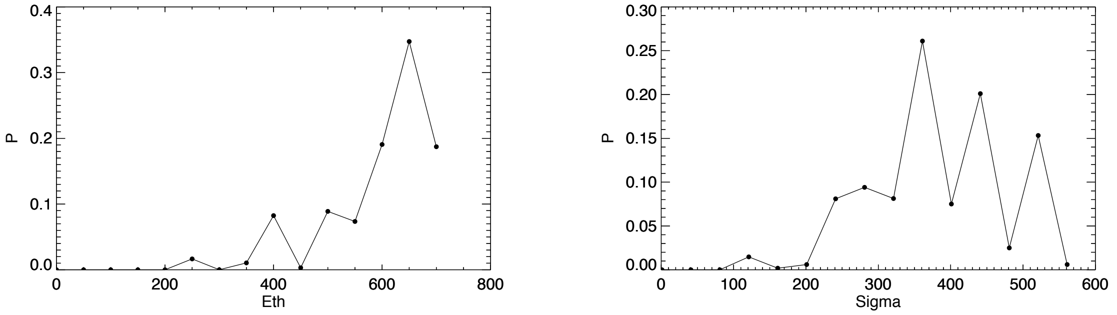

(c) $P(E_R)$ **(d)** $P(\sigma)$

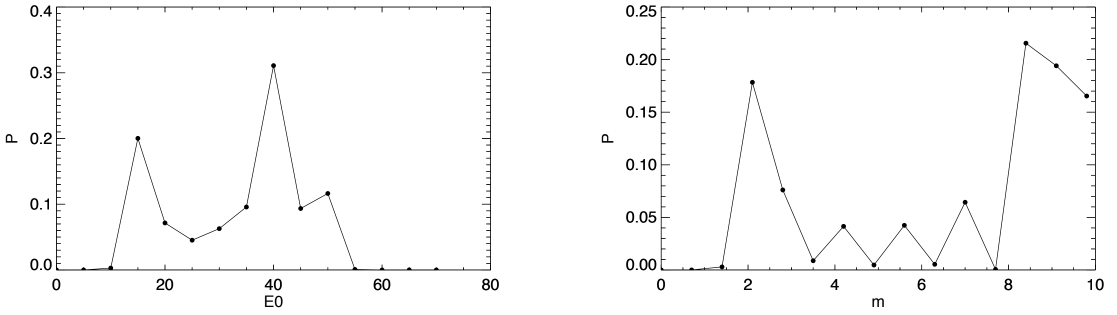

(e) $P(E_0)$ **(f)** $P(m)$

Figure 4.1: Likelihood profiles individual parameters in the model

The individual distributions of an exemplary data set (FEE 1, Loop 1, Revolution 1916) resulting from this process can be seen in Fig. 4.1. Ideally every distribution should resemble a gaussian function, but this is not the case for any parameter except for α. The distribution for α (Fig. 4.1b) is determined quite well with the fitting model. All other distributions (Fig. 4.1 a,c,d,e,f) have irregular shapes with no distinguished peak and can therefore not be uniquely determined. This demonstrates a high correlation between the parameters and a degeneracy of the model for which reason the model needs to be constrained.

4.2 Constrained Model Fits

In the following analysis, a model constrain is set with the aid of the Earth calibration, even though the calibration may have drifted during the 16 mission years. The parameters E_0 and m are now being fixed on the calibration values from Earth and the resulting model then contains four free parameters. By assuming the calibration remained constant over time, a potential change in the detector's response, i.e. a change in E_R and σ, can be investigated. The model is first tested on various data examples. As a test example the data set from FEE 11 of the first calibration period at revolution 209 is chosen, because the calibration values for E_0 and m should be more accurate for an early revolution. The data set of all loops are fitted simultaneously, because the data sets of the loops are gathered in a rather short period of time in which the parameters of the model are expected to not vary significantly, meaning the data does not vary more than due to their Poisson distribution. Especially solar activity, which has the biggest influence on the data, can be viewed as constant during the measurement time. The resulting fit can be seen in Fig. 4.2a.

In order to test the goodness of the fit, the reduced chi-squared statistic can be used. As already described, the fitting method minimizes the conventional χ^2 and its lowest value defines the best fit. The absolute value of χ^2 is depends on the numbers of data points and gives no insight whether the model actually resembles data well. A convenient indicator for this is the reduced chi squared, χ^2_ν, which includes the degrees of freedoms of a fit. The degrees of freedom ν are defined by the difference of the number of data points n_1 and the number of fitted parameters n_2: $\nu = n_1 - n_2$. The reduced chi squared is given by the conventional χ^2 divided by the degrees of freedom:

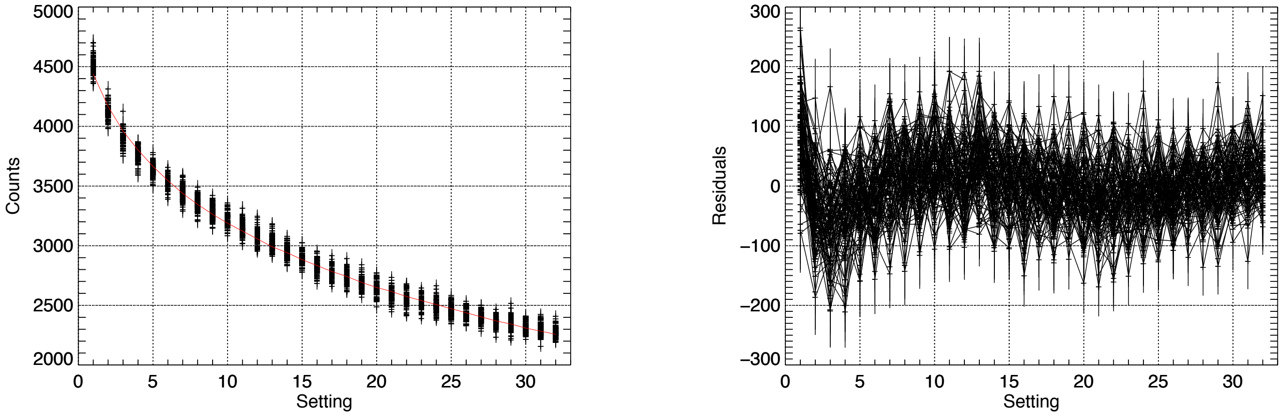

(a) Fitted data of all individual loops

(b) Residuals of the fit

Figure 4.2: Fitted data from FEE 11, revolution 209 and the resulting residuals

$$\chi^2_\nu = \frac{\chi^2}{\nu} \tag{4.6}$$

A good fit results in an expectation value of 1 for χ^2_ν. A value higher than 1 indicates that the model is not fully describing the data and a value lower than 1 indicates that the model is overfitting the data. The standard deviation of the reduced χ^2-distribution is given by:

$$\Delta\chi^2_\nu = \sqrt{\frac{2}{\nu}} = 0.04 \tag{4.7}$$

The fit of Fig. 4.2a results in a χ^2_ν value of 1.17. So the resulting χ^2_ν is still about four standard deviations off its aimed expectation value, which means the model does not describe the data sufficiently.

This is also shown in Fig. 4.2b. It pictures the residuals of the resulting fit. Due to the high number of data points the image is very crowded, but a general shape still becomes apparent. If the model would match the data well, the residuals would scatter around zero with no recognizable pattern as a consequence of the statistical distribution of the data points. A distinct pattern on the other hand indicates that the model and the data do not fully agree.

As individual loops show the same residual pattern, the mean values of all loops is considered. Instead of fitting all loops at once, the mean value of the counts $\langle C\rangle$ for each settings is calculated, which result in single value for each setting. The uncertainty is given by $\Delta\langle C\rangle = \sqrt{\frac{\langle C\rangle}{N_{loops}}}$ due to gaussian propagation of uncertainty. The number of loops per calibration period is given by N_{loops}. The resulting fit can be seen in Fig. 4.3a. The χ^2_ν of the fit now is 8.7, which clearly indicates that the model

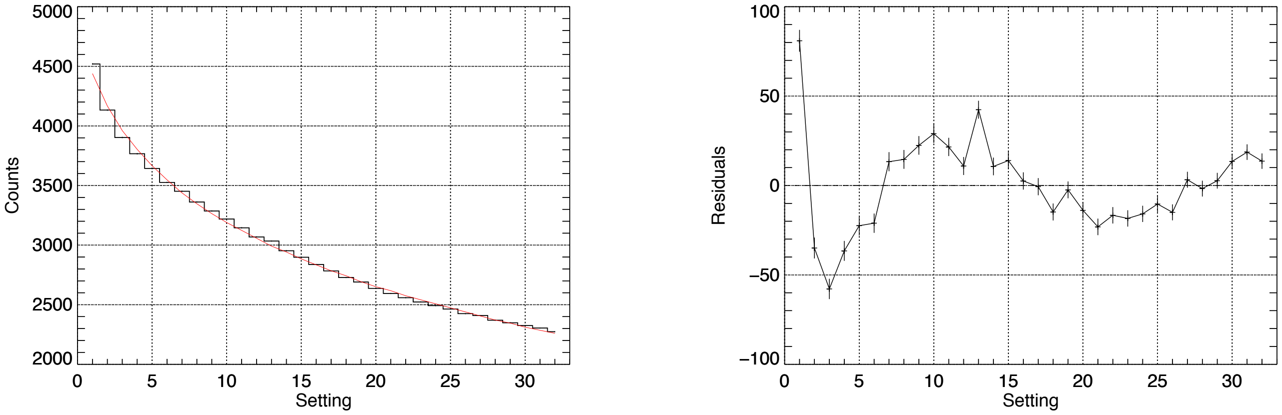

(a) Fitted mean values of all loops

(b) Residuals of the fit

Figure 4.3: Fitted mean values of the data from FEE 11, revolution 209 and the resulting residuals

does not resemble the data good enough. The discrepancy can be seen in Fig. 4.3b, which pictures the residuals. For low setting numbers the model gives too large values and for setting numbers between around 5 and 15, a distinct, broad, peak can be seen. Between setting 15 and 25 the residuals drop again and for setting numbers higher than 26 they rise again. This deviation pattern is larger than a statistical fluctuation and not erratic.

In order to check if this discrepancy is an exception or also appears on other FEEs, the fitting process is applied to other FEEs in the same revolution. As an example, Fig. 4.4 shows the residual pattern of 5 FEEs from different position on the ACS. The x-axis of the plot now resembles energy instead of setting. For the conversion from setting to threshold energy the Earths calibration values were used. Because each FEE has a different calibration, the energy range is different for different FEEs. This way, different FEEs can be compared and it can be checked if the discrepancies are occurring at the same energies. A collective behavior becomes apparent. The residuals peak at around 200 keV, drop after that and rise again for higher energies. A similar behavior can be observed for most of the other FEEs. Fig. 4.5 displays the residuals obtained with the same method for all FEEs from number 1 to 35 and from 55 to 90. There are no documented calibration values for FEEs 36 to 54 (von Kienlin, 2018, priv. comm.). Some deviate strongly from the average residual curve, which is probably caused by changes in the Earth calibration until now.

A common discrepancy suggests that there is an aspect in the data emergence, which the model does

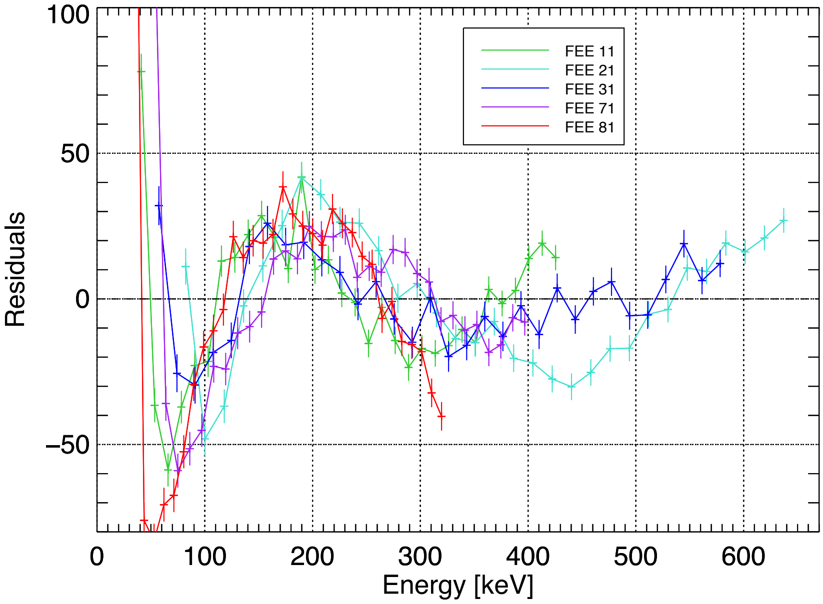

Figure 4.4: Residuals of the fitted mean values for five example FEEs

not cover adequately.

In general, the model is constructed from three assumptions: a power law for the cosmic-ray spectrum, an error function for the response and a linear relation for the calibration. In the following, we consider the cosmic-ray spectrum to be least-accurately modeled, and perform model tests of different shapes.

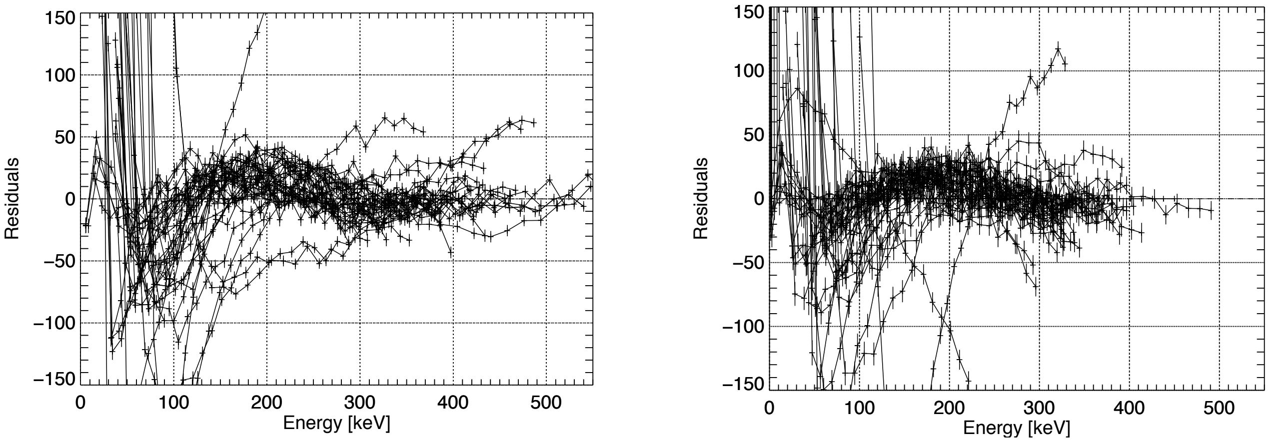

(a) FEE 1-35

(b) FEE 55-90

Figure 4.5: Residuals of the fitted mean values from revolution 209

4.3 Modeling the Low-Energy Cosmic-Ray Spectrum at the INTEGRAL-orbit

As a base-line model, a conventional power law (see equation 3.1 and Fig. 4.6a) was used to approximate the cosmic ray spectrum, but the results of the previous section suggests that the cosmic-ray spectrum could be different. There a many options for how such a spectrum could differ from a power law. In the following sections, additional assumptions on the shape of the cosmic-ray spectrum are tested and compared to the base-line model using the χ^2-test statistic.

4.3.1 Alternative Models for the Cosmic-Ray Spectrum

One other option to model the cosmic-ray spectrum is the sum of two conventional power laws. The basic shape is rather similar to just one power law but the function has a better capability to describe slight changes in the slope of the cosmic-ray spectrum. Its general function can be seen in Fig. 4.6b and is given by:

$$F(E) = A_1 \cdot E^{\alpha_1} + A_2 \cdot E^{\alpha_2} \tag{4.8}$$

In using a cutoff power law for low energy values, a shape similar to a conventional power law but with a drop after a certain threshold value E_c, can be modeled. This behavior is achieved by an additional exponential factor. For the cosmic-ray spectrum there are two plausible candidates: a cutoff power law added to a conventional power law and the sum of two cutoff power laws. They are portrayed in Fig. 4.6c and 4.6d. The first option can be parameterized as follows:

$$F(E) = A_1 \cdot E^{\alpha_1} \; + A_2 \cdot E^{\alpha_2} \, e^{-\frac{E}{E_c}} \tag{4.9}$$

The sum of two cutoff power laws is therefore given by:

$$F(E) = A_1 \cdot E^{\alpha_1} \, e^{-\frac{E}{E_{c,1}}} \; + A_2 \cdot E^{\alpha_2} \, e^{-\frac{E}{E_{c,2}}} \tag{4.10}$$

A potential sudden change in the spectral index and therefore its slope on a logarithmic scale can be described with a broken power law. In this case the spectrum breaks to a higher or lower index after a certain threshold value E_b. This behavior can be expressed with a piecewise defined function:

$$F(E) = \begin{cases} A \cdot E^{\alpha_1} & \text{for } E < E_b \\ A \cdot E_b^{\alpha_1 - \alpha_2} \cdot E^{\alpha_2} & \text{for } E \geq E_b \end{cases} \tag{4.11}$$

An example of this function is pictured in Fig. 4.6e. Another intriguing alternative is that additionally to a continuous spectrum the flux of a specific gamma-ray line adds to the spectrum. These can either have a cosmic origin (e.g. the positron annihilation line at 511 keV) or originate from the spacecraft itself. As Fig. 4.4 shows, most residuals peak at around 200 keV. A potential source for this behavior could be the gamma-ray line at 198 keV from the de-excitation of a ^{71}Ge state caused by neutron irradiation (Jean et al., 2003). Since SPI's camera is composed of 19 germanium detectors, this line is strong and could have a relevant impact on the spectrum received by the ACS. Due to the poor energy resolution of BGO crystals, the line would also be broadened enough to account for a discrepancy in the form of a wide peak as observed. In general this behavior can be described by a power law and a gaussian function centered at an energy value E_p. It can be seen in Fig. 4.6f and is expressed by:

$$F(E) = A_1 \cdot E^{\alpha} + A_2 \cdot e^{-\left(\frac{E - E_p}{\sqrt{2}\sigma}\right)^2} \tag{4.12}$$

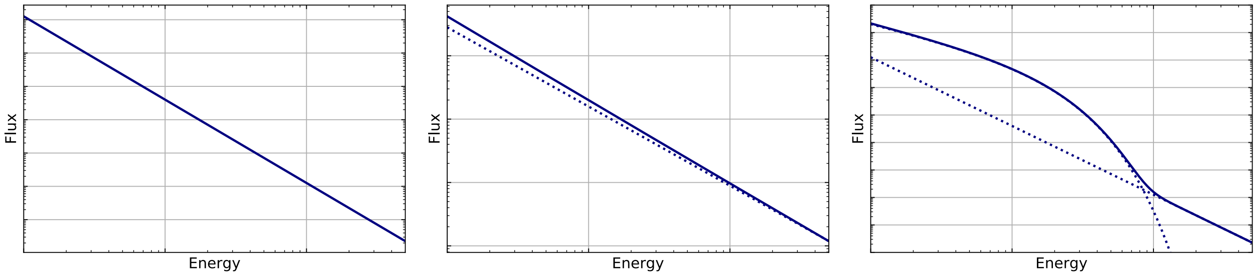

(a) Conventional power law

(b) Power law + power law

(c) Cutoff power law + power law

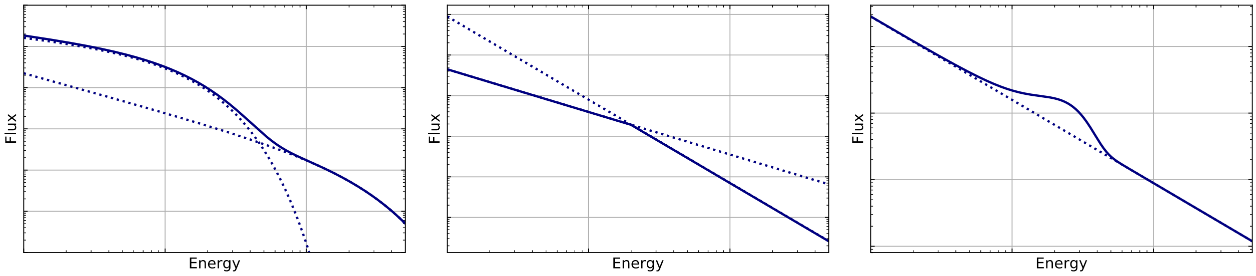

(d) Cutoff power law + cutoff power law

(e) Broken power law

(f) Power law + gaussian peak

Figure 4.6: Possible models for the cosmic-ray spectrum

4.3.2 Comparing the Models

Now it is tested whether these alternatives improve the model, and if so on which level. It also needs to be investigated whether the received spectrum is different for individual FEEs. Each component of the ACS is tested individually by choosing FEEs in the shadow of INTEGRAL, FEEs more aligned to the sun and orthogonal to it.

Most of the counts measured by the ACS are produced by particles with energies lower than 10 MeV, i.e. the biggest influence for the cosmic-ray spectrum striking the ACS is the sun. So if there is a difference in the kind of spectrum received by individual FEEs, it should be caused by a difference in exposure and orientation on the spacecraft. INTEGRAL is always equally aligned towards the sun. If a conceptual z-axis is placed through SPI and IBIS or orthogonal to the solar panels, the +z direction always points towards the sun. One side of the ACS is therefore constantly facing the sun with IBIS in between. This means the BGOs are differently occult by the spacecraft and exposed to solar cosmic rays. This may result in a difference in the received spectrum by the FEEs, and is investigated by modeling the spectrum of six FEEs (three FEEs monitoring BGOs facing the sun, three FEEs monitoring BGOs averted from the sun) from the upper-collimator ring (UCR), six FEEs (also three for each orientation) from the lower-collimator ring (LCR) and three FEEs from the lower-veto shield (LVS). The BGOs chosen from the LVS are located at the "bottom" of SPI and their main surface is aligned parallel to the z-axis.

The data sets from the first calibration period are fitted with every discussed model for all selected FEEs. The degrees of freedom of the individual models and the resulting χ^2_ν values for all fits are displayed in Table 4.1. For almost all FEEs the sum of a cutoff power law and a power law results

Table 4.1: Resulting χ^2_ν values for the data set of revolution 209

		Power law (P.L.)	P.L.+P.L.	Cut. P.L. + P.L.	Cut. P.L. +Cut. P.L.	Broken P.L.	P.L.+line
	ν	28	26	25	24	26	25
UCR (-z)	FEE1	8.09	7.98	**1.69**	3.02	2.34	7.55
	FEE7	48.78	46.62	**5.47**	8.48	12.01	11.69
	FEE13	2.05	2.12	1.26	1.94	**0.62**	1.30
UCR (+z)	FEE4	6.26	2.34	**2.31**	3.82	3.14	5.11
	FEE10	9.78	8.43	**3.02**	6.16	8.98	10.01
	FEE16	267.11	269.67	**12.2**	22.09	128.79	84.18
LCR (-z)	FEE19	293.72	307.12	**32.4**	32.76	224.03	158.55
	FEE25	2.54	2.62	**0.92**	6.99	2.05	3.08
	FEE31	2.72	2.60	2.18	3.45	2.37	**2.14**
LCR (+z)	FEE22	14.69	15.13	**2.55**	8.95	9.81	16.04
	FEE28	5.48	4.64	5.46	**2.81**	5.17	5.57
	FEE34	14.32	14.55	15.39	**2.17**	14.13	15.28
LVS (x)	FEE82	15.15	15.64	**2.37**	4.84	12.51	17.28
	FEE84	8.69	9.20	**2.54**	3.09	7.33	6.39
	FEE88	0.85	0.90	**0.74**	3.27	0.711	0.90

in the best improvement of the base-line model. The best improvements for the individual FEEs are marked in bold. However, the fit is still far away from optimal, with χ^2_ν taking mostly values between 1 and 3 and often even higher, which indicates that the model still lacks accuracy and does not fully agree with the data.

A possible flaw could be created by using the calibration values obtained at Earth. They might not be accurate enough to be used for a data analysis and therefore cause a descrepancy of the model. This could be caused for example by a difference in temperature. The ACS was calibrated at room temperature at Earth, but is operating at a much lower temperature in space. This could have a considerable influence on the detector's response and could therefore distort the desired value of the energy threshold. Moreover, the ACS was calibrated with de-excitation gamma rays from radioactive sources. However most of its data obtained in space is produced by cosmic rays, meaning mostly protons and heavier nuclei, for which the detector's response could be different. For these sources, therefore, the calibration's accuracy might be reduced. Furthermore, the underlying assumption of a linear relation for the calibration might be inaccurate. The energy thresholds could in general not be equidistant, which impairs the whole model. However, the Earth calibration values are required to constrain the model, so it does not become unambiguous and looses its validity. Another inaccurateness could potentially be created by the model function for the response. It approaches high detection probabilities for high energies, without decreasing after a certain energy value, which needs to be incorporated in a more realistic model. The relevance of this decline may have been underestimated. The extraordinary high values of FEE 16 and FEE 19 are probably due to outliers in the data caused by interfering events. The method of least squares is quite sensitive towards outliers and can therefore produce exceptional high χ^2_ν values. Furthermore, no significant difference in the kind of spectrum received by the FEEs can be observed. So FEEs monitoring BGOs with different positions on the spacecraft, and therefore different exposure towards the sun, can be analyzed with the same model.

The improvement of the alternative model shows that the conventional power law is not sufficient to model the cosmic-ray spectrum. Since the sum of a cutoff power law and a power law achieves the best improvement, it will be used in the further analysis.

4.4 Changes of the Response over Time

4.4.1 Comparing Time-dependent and Time-independent Models with the χ^2 test

The further goal of the analysis is to investigate whether the response has changed and if this change has a significant influence on the data. Hence data sets of all calibration periods of one individual FEE are now fitted simultaneously. The comparison of the models is achieved by a hypothesis test. The hypothesis represented by the first model can be formulated as:

$$H_0 : There\ is\ no\ significant\ continuous\ change\ in\ the\ detector's\ response$$

In this time-independent model, E_R and σ are set constant over time. Due to the solar cycle, the cosmic-ray spectrum can vary its intensity, but not its shape. The resulting model then equals:

$$C_i(s) = 0.5 \int_{E_0+m\cdot s}^{\infty} \left(A_{1,i} \cdot E^{\alpha_1} + A_{2,i} \cdot E^{\alpha_2}\, e^{-\frac{E}{E_c}}\right) \left[\operatorname{erf}\left(\frac{E-E_R}{\sigma\sqrt{2}}\right)+1\right] \mathrm{d}E \tag{4.13}$$

The index i determines the number of calibration period. Hence A_1, A_2, which represent intensities, are fitted individually for each calibration period. All other parameters are fitted to a constant value collectively. E_0 and m again are fixed on the values obtained by the Earth calibration.
The second model represents the following hypothesis:

$$H_1 : There\ is\ significant\ continuous\ change\ in\ the\ detector's\ response$$

It incorporates a change over time of E_R and σ. Because there is no prior information of how they would potentially change, a linear relation marks a valid first order approximation. So the two parameters are parameterized by:

$$E_R(t) = E_{R,0} + E_{R,1} \cdot t \tag{4.14}$$

$$\sigma(t) = \sigma_0 + \sigma_1 \cdot t \tag{4.15}$$

The complete time-dependent, second model therefore is:

$$C_i(s,t) = 0.5 \int_{E_0+m\cdot s}^{\infty} \left(A_{1,i} \cdot E^{\alpha_1} + A_{2,i} \cdot E^{\alpha_2}\, e^{-\frac{E}{E_c}}\right) \left[\operatorname{erf}\left(\frac{E-(E_{R,0}+E_{R,1}\cdot t)}{(\sigma_0+\sigma_1\cdot t)\sqrt{2}}\right)+1\right] \mathrm{d}E \tag{4.16}$$

In order to investigate a potential change over time, the time-independent model is fitted to the data first. Then the time-dependent second model is fitted and by applying a χ^2 test, an improvement can be quantified. If there is a significant change of the detector's properties, the time-dependent model should result in a better fit.
In order to apply the fitting model, the data sets of all calibration periods are sequenced in chronological

order. This way some parameters can have a collective value while the intensity can vary. Fig. 4.7 shows such a plot of the data and the resulting fit for FEE 1. The periodic rise and fall of the intensity over time is due to the solar cycle. During times of high solar activity, the cosmic-ray flux decreases and rises for low solar activity, as explained earlier. The displayed fitted function in red was determined by the time-independent model. The x-axis forms a continuous domain for all data sets, as the the setting range (1:32) is multiplied by the number of calibration periods, which range from 1 to 24. The two discussed models result in χ^2 values of:

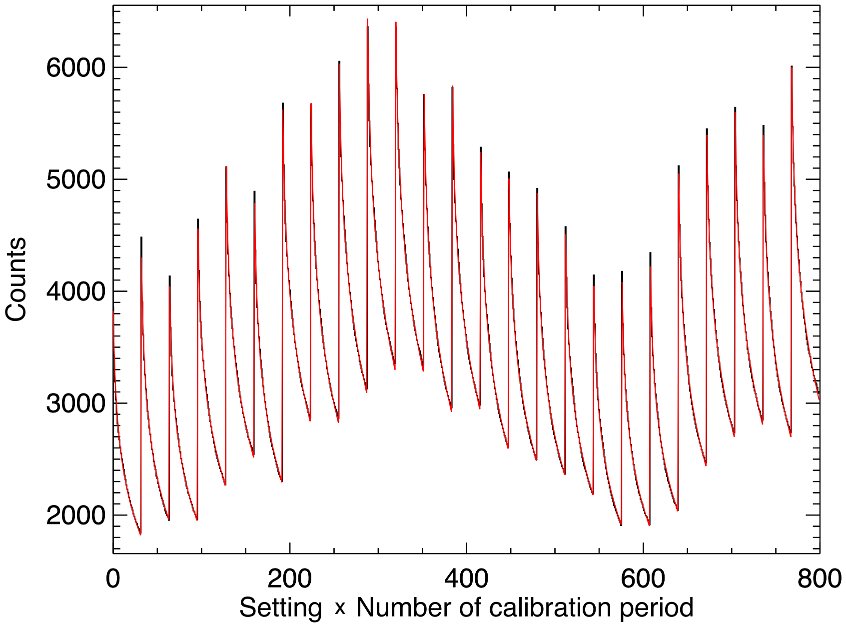

Figure 4.7: Data sets from FEE1 for all calibration periods fitted with the time-independent model

$$\chi^2_{(H_0)} = 11513 \qquad\qquad \chi^2_{(H_1)} = 11417$$

The time-dependent model gives a smaller χ^2 and therefore provides a better fit to the data. Applying a Pearson's χ^2 test, results in a significance level of 9.5σ. This would be a highly significant result, however it needs to be treated with caution. Despite the alteration of the cosmic-ray spectrum the fit is still insufficient. The associated χ^2_ν values are far from optimal:

$$\chi^2_{\nu(H_0)} = 15.55 \qquad\qquad \chi^2_{\nu(H_1)} = 15.42$$

The χ^2 test evaluates the absolute difference of both χ^2 values and since both fits are insufficient the difference can become relatively large. This shows that, if both models are too inadequate, they cannot be used for comparison. Consequently a model based approach for comparison does not achieve a solid result.

4.4.2 Comparing the Data with the Kolmogorov-Smirnov Test

In general a Kolmogorov-Smirnov (KS) test (Press et al., 1992, Chapter 14) can be used to examine if two data samples were drawn from the same distribution. The great advantage thereby is, a KS test is a model independent approach and can therefore be directly applied to the data. The underlying idea is that a potential change over time in the detector's properties should show a change in the shape of the data. The data set obtained at revolution 209 after launch, which is the first revolution in which calibration data was gathered, serves as an reference of comparison. The KS test can then check if data sets from other calibration periods arise from a similar distribution. In this way a change over time can be quantified.

In the case of the ACS data, the probability distribution is given by the cosmic-ray spectrum or rather the cosmic-ray spectrum convolved with the response function. A potential change over time of detector responses would therefore influence this distribution. A KS test compares cumulative distribution functions of two data sets. An empirical distribution function is a step function depending on a random variable X, which gives the cumulative probability at a certain value x. This is the probability that X takes on a value less than or equal to x:

$$F(x) = P(X \leqslant x) \tag{4.17}$$

It therefore results in values between 0 and 1. The calibration data of the ACS is of the form of such function, but is not normalized. A run through all possible detector settings samples the cumulative distribution function with 32 points, since the integral over the spectrum represents the unnormalized cumulative probability. So if the data of one calibration period is normalized to a codomain between 0 and 1, it resembles the desired function. This is achieved by a linear transformation. A data set (mean values for all settings of one FEE) containing C counts, is normalized by the highest (C_{max}) and lowest (C_{min}) recorded counts among the settings:

$$C_{normalized} = \frac{C - C_{min}}{C_{max} - C_{min}} \qquad \in [0;1] \tag{4.18}$$

Fig. 4.8 displays an example of such normalized data sets obtained from FEE 1. The reference data set is marked in red. The function runs from 1 to 0 opposed to a conventional distribution function, but for the KS test this is irrelevant. The null hypothesis, "No significant change over time" , is tested via the KS test. This hypothesis can also be formulated as follows, where C_0 resembles the data from the first calibration period after launch and C_1 the data to be tested :

$$H_0 : C_1 \; is\ drawn\ from\ the\ same\ distribution\ as\ C_0$$

The result of the KS test equals a probability p for the emergence of both data sets, given H_0 is true. This probability is calculated via the test statistic D. It equals the maximum difference between the two compared distribution functions in y-direction, meaning the biggest difference of cumulative probability for a mutual setting. The probability p is approximately given by:

$$p(D) = Q_{KS}\left(\left[\sqrt{N_e} + 0.12 + 0.11/\sqrt{N_e}\right] D\right) \tag{4.19}$$

whereas Q_{KS} is defined as

$$Q_{KS}(\lambda) = 2\sum_{j=1}^{\infty}(-1)^{j-1}\, e^{-2j^2\lambda^2} \tag{4.20}$$

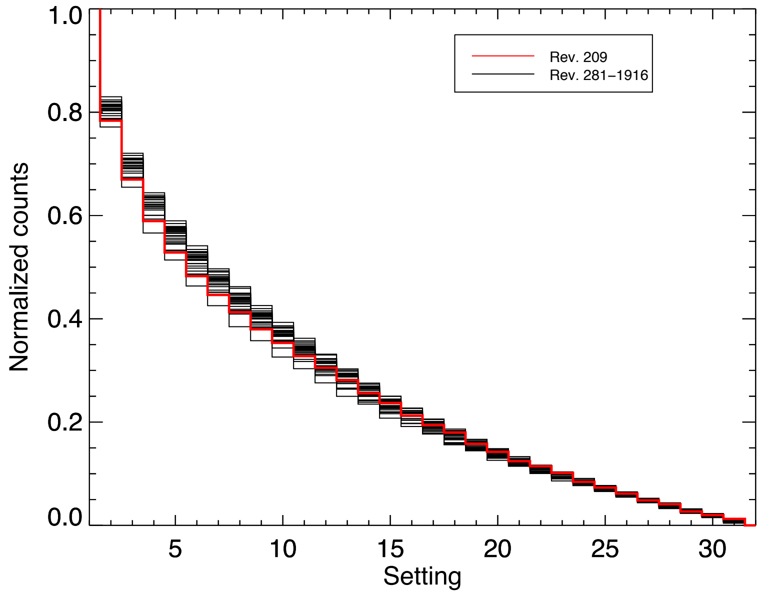

Figure 4.8: Normalized data of all revolutions from FEE 1

and N_e is the effective number of data points. The KS test compares two data sets emerging from different number of loops. Hence they have different numbers of data points (N_1, N_2) and an effective number of points has to be used (Press et al., 1992, p. 619), which is given by:

$$N_e = \frac{N_1 \cdot N_2}{N_1 + N_2} \tag{4.21}$$

The number of data points is determined by the rate in which the ACS is gathering its data. As mentioned before, the FEEs are read out every 50 ms and during a loop a setting is set for 5 s. Hence a single value of counts for one setting in a loop is produced by $N_0 = \frac{5\,\mathrm{s}}{50\,\mathrm{ms}} = 100$ data points. The data sets examined contain the mean values of all loops. The whole number of data points creating the empirical distribution functions, therefore, equals the number of points per loop times the number of loops performed in this particular calibration period:

$$N_i = N_0 \cdot N_{loops} = 100 \cdot N_{loops} \tag{4.22}$$

Putting it all together the probability p can be determined. A low value for p indicates that the data sets are quite different in their shape. This can also be expressed in terms of a normal distribution even though the distribution functions are not normal. A significance level of 1σ then resembles a 31.7 % chance for the data emergence given H_0. 3σ would represent a 0.27 % chance and so on. A high σ value, therefore, corresponds to a big difference in shape between the data sets.

This procedure is now applied to the data of all FEEs, which gives significance levels for each calibration period compared to the first calibration run. In general the FEEs produce vastly different patterns and there is no observable overall collective behavior. However similarities show up for some FEEs. Fig. 4.9a contains the shifting of the significance level over time for six FEEs. The FEEs produce a pattern with two periodic peaks, similar to the solar cycle. In times of higher cosmic-ray flux, the data sets differ more from the first one. This would indicate that solar activity would not only affect the intensity of the cosmic-ray spectrum but also its shape. It is unlikely that such pattern is caused solely by a change of the detector's properties. Some other FEEs produce a steadily growing change of spectral appearance over time, meaning the shapes of the data sets match less and less over time with the first calibration data set. Fig. 4.9b shows six examples for such behavior. This could be caused by a continuous change of the detector properties, e.g. a degradation of the crystal's light yield or an alteration of the electronics. A few FEEs also show a decline of the significance levels for the latest calibration periods. This pattern is even more distinct for some other FEEs, as can be seen in Fig. 4.9c. The FEEs form a strong peak for later revolutions, which is entirely opposed to Fig. 4.9a. Some other FEEs also form patterns that do not fall in any of the mentioned groups. There is no apparent correlation between the arising pattern and the position of BGOs on the spacecraft. FEEs monitoring neighboring BGOs can result in vastly different patterns. The variation of patterns can therefore not be explained by a difference in exposure towards the sun or orientation on the spacecraft.

Nevertheless, a commonality for all FEEs is that they all show a general significant change. Almost all current significance levels obtained from revolution 1916 are above 3σ, meaning the probability for the data emergence given the distribution is the same for both revolutions is under 0.3%. Values in between are even higher with peaks at 14σ. This makes H_0 unlikely for all FEEs. Hence is seems that the ACS data is changing significantly from the first calibration data set over time due to a variation in the response of the detectors. Solar activity can also be an additional influential factor, but the patterns are too diverse. The suns influence would be collective and therefore cannot solely account for the change.

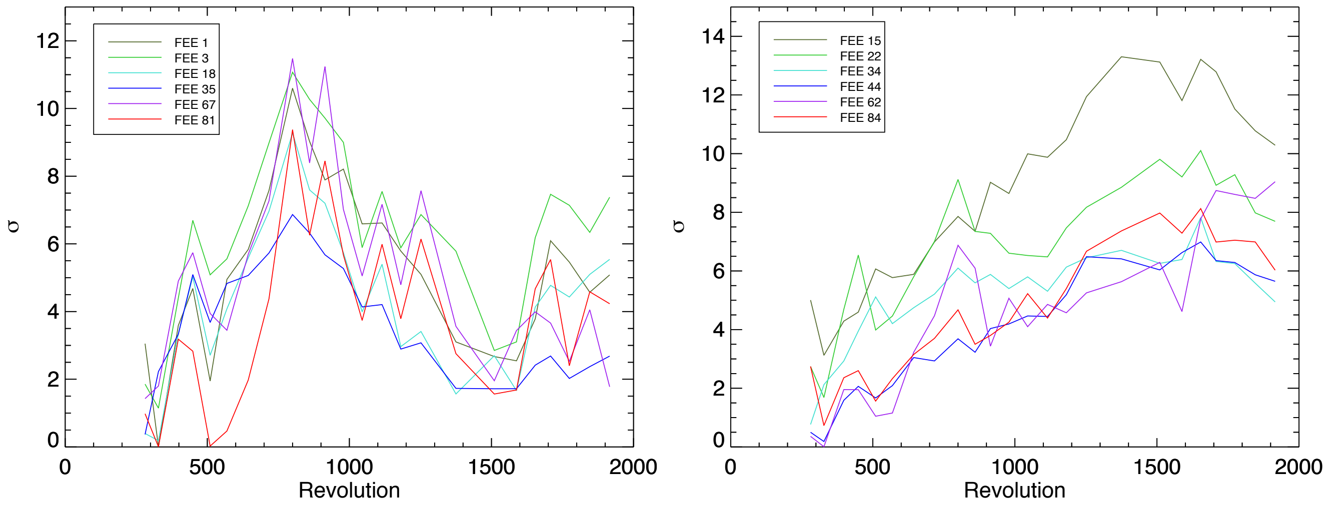

(a) Pattern with similiarities to the solar cycle

(b) Steadily growing change of spectral appearance

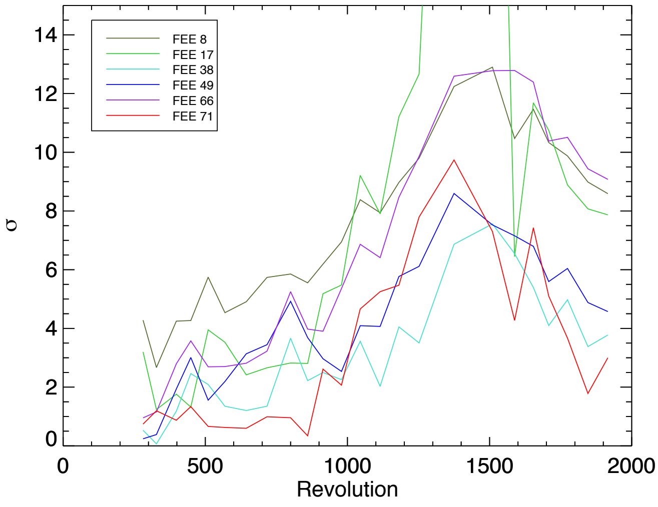

(c) Peak-like pattern of the significance levels

Figure 4.9: Significances obtained with the KS test of several FEEs for all calibration periods

5. Summary and Conclusion

In this thesis, data from the SPI-ACS was analyzed towards a better understanding of the performance scintillation detectors in a long duration space environment. The goal was to examine the behavior of the detector's response, the received spectrum and to investigate the possibility of a new calibration. The data used to address these questions had been gathered every half a year during the 16 years of INTEGRAL's mission and contains cumulative count rates for different energy threshold settings of the ACS.

In order to exploit this data, a model was developed, which aims to parameterize the process of data emergence. It is based on assumptions about the incoming cosmic-ray spectrum, the detectors response and the calibration. Because this model turned out to be highly degenerate, it had to be constrained by using the Earth calibration. This makes a renewal of the calibration much more complex, and only qualitative statements about changes were possible. Hence the further analysis addressed the question, whether something in the response has changed in general, and how the ACS components can be characterized over time. The constrained model describes the ACS data as if the calibration did not change after the launch of INTEGRAL and accounts for variation in the response and received spectrum. This resulted in a not fully consistent description of the the data. In particular, it showed a systematic discrepancy from the data at energies around 200 keV. This indicates that additional features are required over a simple power-law approximation. Attempts to improve the model, by using several other assumptions about the cosmic-ray spectrum, were tested. Improvements in the fit quality were significant, but the model remained insufficient to explain the full spectrum. Therefore, a model based approach for the investigation of significant changes over time was based on too weak assumptions and was not able to give solid results.

The last part of the analysis presented in this thesis focused on a model independent approach. In order to determine qualitative changes in the ACS data over time, a Kolmogorov-Smirnov test was applied to the data as a normalized cumulative distribution function. In general, after 16 mission years, the shape of the ACS data appears to have change significantly from the first calibration data set, serving as a reference. The test solely evaluated data obtained in space, and therefore does not capture potential changes due to the different environment in space or the launch of INTEGRAL. These insights increase the necessity of a tuning of the ACS, but make no quantitative statement about how much the current calibration and therefore the energy thresholds for individual FEEs are off. In order to actually perform a new calibration, the correct relation between setting and energy threshold as well as the current parameters of such relation would have to be precisely determined in some way. Alternatively a relative calibration rather than using absolute values might be an option.

Bibliography

B. P. Abbott, R. Abbott, T. D. Abbott, F. Acernese, K. Ackley, C. Adams, T. Adams, P. Addesso, R. X. Adhikari, V. B. Adya, and et al. Gravitational Waves and Gamma-Rays from a Binary Neutron Star Merger: GW170817 and GRB 170817A. *ApJL*, 848:L13, October 2017. doi: 10.3847/2041-8213/aa920c.

D. Attié, B. Cordier, M. Gros, P. Laurent, S. Schanne, G. Tauzin, P. von Ballmoos, L. Bouchet, P. Jean, J. Knödlseder, P. Mandrou, P. Paul, J.-P. Roques, G. Skinner, G. Vedrenne, R. Georgii, A. von Kienlin, G. Lichti, V. Schönfelder, A. Strong, C. Wunderer, C. Shrader, S. Sturner, B. Teegarden, G. Weidenspointner, J. Kiener, M.-G. Porquet, V. Tatischeff, S. Crespin, S. Joly, Y. André, F. Sanchez, and P. Leleux. INTEGRAL/SPI ground calibration. *A&A*, 411:L71–L79, November 2003. doi: 10.1051/0004-6361:20031302.

A. Balogh, H. S. Hudson, K. Petrovay, and R. von Steiger. Introduction to the Solar Activity Cycle: Overview of Causes and Consequences. *SSR*, 186:1–15, December 2014. doi: 10.1007/s11214-014-0125-8.

V. Blobel and E. Lohrmann. *Statistische und numerische Methoden der Datenanalyse*. 1998. doi: 10.1007/978-3-663-05690-4.

A. De Angelis and M. Pimenta. *Introduction to Particle and Astroparticle Physics*. Springer, 2015.

R. Diehl. Nuclear astrophysics lessons from INTEGRAL. *Reports on Progress in Physics*, 76(2): 026301, February 2013. doi: 10.1088/0034-4885/76/2/026301.

M. Gros, V. Tatischeff, J. Kiener, B. Cordier, C. Chapuis, G. Weidenspointner, G. Vedrenne, A. von Kienlin, R. Diehl, A. Bykov, and M. NMéndez. INTEGRAL/SPI Observation of the 2003 Oct 28 Solar Flare. In V. Schoenfelder, G. Lichti, and C. Winkler, editors, *5th INTEGRAL Workshop on the INTEGRAL Universe*, volume 552 of *ESA Special Publication*, page 669, October 2004.

T. Hauschild and M. Jentschel. Comparison of maximum likelihood estimation and chi-square statistics applied to counting experiments. *Nuclear Instruments and Methods in Physics Research A*, 457: 384–401, January 2001. doi: 10.1016/S0168-9002(00)00756-7.

P. Jean, G. Vedrenne, J. P. Roques, V. Schönfelder, B. J. Teegarden, A. von Kienlin, J. Knödlseder, C. Wunderer, G. K. Skinner, G. Weidenspointner, D. Attié, S. Boggs, P. Caraveo, B. Cordier, R. Diehl, M. Gros, P. Leleux, G. G. Lichti, E. Kalemci, J. Kiener, V. Lonjou, P. Mandrou, P. Paul,

S. Schanne, and P. von Ballmoos. SPI instrumental background characteristics. *A&A*, 411:L107–L112, November 2003. doi: 10.1051/0004-6361:20031156.

G.F. Knoll. *Radiation detection and measurement.* 2000.

W. H. Press, S. A. Teukolsky, W. T. Vetterling, and B. P. Flannery. *Numerical recipes in FORTRAN. The art of scientific computing.* 1992.

A. Rau, A. von Kienlin, K. Hurley, and G. G. Lichti. The Sample of Gamma-Ray Bursts Observed with SPI-ACS. In V. Schoenfelder, G. Lichti, and C. Winkler, editors, *5th INTEGRAL Workshop on the INTEGRAL Universe*, volume 552 of *ESA Special Publication*, page 607, October 2004.

A. Rau, A. V. Kienlin, K. Hurley, and G. G. Lichti. The 1st INTEGRAL SPI-ACS gamma-ray burst catalogue. *A&A*, 438:1175–1183, August 2005. doi: 10.1051/0004-6361:20053159.

P. A. Sturrock, M. Weber, M. S. Wheatland, and R. Wolfson. Metastable Magnetic Configurations and Their Significance for Solar Eruptive Events. *ApJ*, 548:492–496, February 2001. doi: 10.1086/318671.

G. Vedrenne and J. Atteia. *Gamma-Ray Bursts - The brightest explosions in the Universe.* Springer, 2009.

G. Vedrenne, J.-P. Roques, V. Schönfelder, P. Mandrou, G. G. Lichti, A. von Kienlin, B. Cordier, S. Schanne, J. Knödlseder, G. Skinner, P. Jean, F. Sanchez, P. Caraveo, B. Teegarden, P. von Ballmoos, L. Bouchet, P. Paul, J. Matteson, S. Boggs, C. Wunderer, P. Leleux, G. Weidenspointner, P. Durouchoux, R. Diehl, A. Strong, M. Cassé, M. A. Clair, and Y. André. SPI: The spectrometer aboard INTEGRAL. *A&A*, 411:L63–L70, November 2003. doi: 10.1051/0004-6361:20031482.

A. von Kienlin. Table of ACS calibration data. Technical report, MPE, 2018.

A. von Kienlin, N. Arend, G. Lichti, A. Strong, and P. Connell. Gamma-Ray Burst Detection with INTEGRAL/SPI. *ArXiv Astrophysics e-prints*, July 2004.

C. Winkler, T. J.-L. Courvoisier, G. Di Cocco, N. Gehrels, A. Giménez, S. Grebenev, W. Hermsen, J. M. Mas-Hesse, F. Lebrun, N. Lund, G. G. C. Palumbo, J. Paul, J.-P. Roques, H. Schnopper, V. Schönfelder, R. Sunyaev, B. Teegarden, P. Ubertini, G. Vedrenne, and A. J. Dean. The INTEGRAL mission. *A&A*, 411:L1–L6, November 2003. doi: 10.1051/0004-6361:20031288.